國立交通大學碩士論文

Two Channel Kondo Pseuodap Anderson Model: Quantum Criticality and Universal Scaling

Student: 巫展霈

Advisor: 仲崇厚

Committee:

牟中瑜

陳柏中

朱仲夏

不交叉近似法於雙渠道贋能隙單雜質安德森模型之應用: 量子相變與統一標度律

學生: 巫展霈　　指導教授: 仲崇厚

國立交通大學電子物理系碩士班理論物理組

摘要

所謂的量子相變 (quantum phase transition) 是指在絕對零度經由調整某些參數所以引起的基態的連續相變。然而這些相變是因爲量子擾動而非熱擾動。另一方面, 近藤效應 (Kondo effect) 也是凝態物理中的重要課題, 它是一個磁性雜質被電子自旋屏蔽而引起的物理現象。因爲奈米科技的進步, 近藤效應在量子點 (quantum dot) 系統的想法得以實現, 也因此, 與近藤效應破滅相關的量子臨界現象 (quantum criticality) 也變成了重要的課題。如果我們可以讓磁性雜質同時和兩個獨立的電子庫耦合, 雙渠道的近藤效應 (two-channel Kondo) 就能被實現。雙渠道的近藤效應會造成非費米液體行爲 (non-Fermi liquid), 這是有別於一般費米金屬的行爲。本論文中, 我們使用的是雙渠道贋能隙安德森雜質模型 (two-channel pseudogap single impurity Anderson model), 所謂的贋能隙能態密度 (pseudogap density of states) 就是能態密度 ($\rho(\omega) \sim |\omega|^r, 0 \leq (r \leq 1)$ 在接近$w = 0$時會呈現冪次方的消逝。然而贋能隙能態密度的指數 r 也分別對應不同的磁性物質參雜材料, 例如加入磁性雜質的石墨稀 (doped graphene) 就是對應 r=1, 而常數能態密度則對應 r=0。如果指數 r 過於大, 能態密度會消失過快而沒有足夠的電子去屏蔽雜質, 因此雙渠道的近藤效應會破滅, 取而代之的是矩限態 (local moment, LM). 只要 r 夠小的話, 系統就會停留在雙渠道的近藤效應基態 (two-channel Kondo ground state)。我們研究雙渠道贋能隙安德森雜質模型 ($0 \leq (r \leq 1)$ 在化學能爲零 ($\mu_0 = 0$) 的情況下, 靠著調整指數 r 來觀察雙渠道近藤效應和矩限態的量子相變。我們只用 slave-boson 大 N 近似法 (large N approach) 去自洽的解雜質電子的格林函數, 其中我們忽略所有有不交叉的費曼圖, 所以又稱不交叉近似法 (NCA)。從磁性雜質的能態密度, 我們可以觀察到量子臨界點 ($r = r_c$), 更進一步的, 同時在平衡態和非平衡的導電度 (conductance) 上找出統一標度律 (universal scaling)。本論文可以提供未來研究非費米液體及量子臨界行爲的理論基礎。

關鍵字:

近藤效應、雙渠道近藤效應

贋能隙、安德森雜質模型

量子相變、統一標度律

不交叉近似法

Non-crossing Approximation Approach To Two Channel Kondo Pseudogap Anderson Model:
Quantum Criticality And Universal Scaling

Student: Jan-Pei Wu Advisor: Prof. Chung hou Chung

Institute of Electric Physics Department
National Chiao Tung University

ABSTRACT

Quantum phase transition (QPT) are the continuous phase transition of ground states by tuning couplings in the quantum system. They are due to zero-temperature quantum fluctuations, not thermal fluctuations. Meanwhile, Kondo effect is an important phenomenon in condensed matter systems, which is an effect describing the screening of magnetic impurity by the spin of conduction electrons in magnetical doped metals. Due the advances in nano-technology, Kondo effect in quantum dots (QD) have been realized in single electron tunneling transistor (SET), therefore QPT associated with the broken down of the Kondo effect becomes an interesting subject. If two independent electron reservoirs exist, two-channel Kondo effect (2CK) becomes possible. It leads to non-Fermi liquid (NFL) behavior, which shows different electric transport from Fermi liquid metals. In our study, we use the 2CK pseudogap Anderson impurity model to describe the system where the single impurity is coupled to 2CK pseudogap electron bath, where its density of states ($\rho(\omega)$) vanishes in a power law fashion ($\rho(\omega) \sim |\omega|^r, 0 \leq r \leq 1$) for $\omega \to 0$. The exponent r of pseudogap density of states varies with different materials. The magnetical doped graphene (r=1) is an example of 2CK pseudogap Anderson single impurity model system, and two-channel quantum dot system with constant density of states corresponds to $r = 0$ case. If r is too large, there is no sufficient electron density of states to screen the impurity spin, 2CK state is broken down, resulting in unscreened local moment (LM) ground state. Let r be small enough, two-channel Kondo effect becomes possible. We study QPT in 2CK pseudogap single impurity Anderson model at zero-chemical potential by tuning r ($0 < r < 1$) both of equilibrium and out of equilibrium. We use slave-boson large-N approach to self-consistently solve Green's functions of electron on the dot by including all non-crossing diagrams, so-called non-crossing approximation (NCA). We extract the quantum critical point (r_c) from impurity density of states, and find the universal scaling both in equilibrium and non-equilibrium conductances near r_c. This thesis provides theoretical basis for further study in Kondo break down, quantum criticality and non-Fermi liquid behavior in condensed matter systems.

Keywords: Quantum Criticality, Quantum Phase Transition, Kondo, two-channel Kondo, Pseudogap, Anderson Model, Universal Scaling

誌謝:

修讀碩士的年頭, 首先要感謝指導仲崇厚教授, 願意教授學生, 傳授知識。另外也要感謝李宗翰學長留下 NCA 數值計算的基礎, 讓我得以繼續研究相關課題。在編寫論文的過程中, 也特別感謝張永業學長對我用 Latex 編寫論文的指導, 還有教授場論基礎。研究室的每一位學長學弟學妹對我的許多幫助, 我都十分感激。要感謝大家在我碩士生涯的幫助, 還有最重要的是我的父母把我養大, 支持我唸研究所, 支付我從小到大的學費, 感恩的心, 到死都不敢忘。最後感謝國立交通大學對我的栽培, 以及完善的教學資源。

List of Figures

1.1 (a) Redline shows resistivity in metals contained magnetic impurities: at low temperature, using third order perturbation theory, Kondo found that this scattering process leads to a lnT behavior in resistivity. Blueline shows resistivity in normal metals. (b) In quantum dot system, Coulomb blockade influence conductance. At low temperature, when temperature decreases, conductance increases (decreases) if electron number is odd (even). Kondo effect appears only odd number, Kondo effect leads to conductance increased at low temperature in QD system. Adapted from [1, 7]. 2

1.2 (a) Kondo effect happened because of impurity screened by spin one half of electrons. Adapted from [58]. (b) Electron-impurity spin-flip scattering. 3

1.3 (a) Scanning electron micrograph of SET device. The top and down electrodes on the left side and the electrode on the right side are used to operate the barrier of quantum dot. The middle electrode on the left side are used to tune the energy level of QD relative to 2DEG [13, 14]. (b) Schematic SET device [21]. 5

1.4 (a) Conductance has two different behaviors at even and odd electron number. (b) The zero bias differential conductance anomaly at $V_{SD} \sim 0$, where V_{SD} is the voltage difference between source and drain. [1, 13, 14]. 6

1.5 The illustration of Coulomb blockade. The first order tunneling is blocked by Coulomb potential U, the cotunneling (2nd) solution is solvable. The additional energy for N to $N+1$ state is $E^2/C + \Delta E$. The voltage spacing between source and drain is defined as V_{SD} which is eV here. 7

1.6 (a) Spin-flip cotunneling process of Kondo effect. (b) The density of states(DOS) of quantum dot, The Kondo resonance lies at the Fermi energy, Kondo effect occurs when the temperature is below the Kondo temperature T_k. Adapted from [21]. 9

1.7 (a) The first order phase transition. Though g_c, the ground state becomes B state from A state with level crossing. (b) The higher order phase transition, avoiding level crossing. The phase transition whose ground state is form A state to B state as g exceeds g_c is a continuous process. Ref. [36] . 10

1.8 (a) The diagram is obtained via the scanning electronic micrograph (STM) in experiment of N. J. Craig *et. al.* [37]. (b) Conductance of left quantum dot. When odd number of electrons on the quantum dot and RKKY antiferromagnetic interaction is stronger than Kondo coupling, Kondo effect will be suppressed by RKKY. Adapted from [37]. 11

1.9 The quantum phase transition coupling K is RKKY coupling, and quantum critical point (QCP) with criticality at zero temperature is located at the K_c. Adapted from [39]. 12

1.10 Quantum phase transition diagram of two-channel Kondo, where $H_{2CK} \sim J_1 S_1(r) \cdot S + J_2 S_2(r) \cdot S$, and J_1, J_2 are Kondo coupling of each channel, respectively. Blue and red phase correspond to blue and red channel in Fig.(1.11), and J_1 (J_2) is the Kondo coupling of red (blue) channel. At zero temperature, one can obtain 2CK state for symmetric coupling. There is still the 2CK state if coupling are some imbalance at finite temperature. The quantum critical region exhibits 2CK non-Fermi liquid behavior at finite temperature. [38] 13

1.11 Two independent electron reservoirs couple to a QD in SET device. Two blue leads and a finite red reservoir represent two independent channel, respectively. Here, red reservoir has to be much large than QD, therefore, there are sufficient electrons to compose a conduction electron band. Two blue leads comes a reservoir which is faraway from QD. Adapted from [16]. 15

1.12 2CK conductance data in 2CK and 1CK scaling, where 1CK scaling follows Fermi liquid $(eV/k_BT)^2$ behavior. 2CK universal scaling follows $(eV/k_BT)^{1/2}$ behavior, not Fermi liquid $(eV/k_BT)^2$, so-called NFL behavior. Adapted from [6, 38]. 16

1.13 The RG flow phase diagram of particle-hole symmetric single impurity pseudogap Anderson model. The details are in text. Adapted from [43]. . . 18

1.14 The RG flow phase diagram of particle-hole asymmetric single impurity pseudogap Anderson model. The details are in text. Adapted from [43]. . . 20

1.15 The RG flow phase diagram of 2CK particle-hole asymmetric single impurity pseudogap Anderson model. The details are in text. Adapted from [44]. 21

1.16 The RG flow phase diagram of 2CK particle-hole asymmetric single impurity pseudogap Kondo model. The details are in text. Adapted from [44]. 23

2.1 The set sup of 2CK pseudogap Anderson model out of equilibrium with strong Coulomb potential. There are two 2CK leads which couple to single QD out of equilibrium, where 2CK leads with pseudogap conduction electron DOS are in thermal equilibrium, respectively. 27

2.2 At lowest order, boson self-energy involves the fermion propagator, and fermion self-energy involves boson propagator. Adapted from [57]. 31

2.3 Diagrammatic self-consistent Dyson's equations, Eq.(2.38)-Eq.(2.41). Adapted from [58]. 34

2.4 The impurity DOS $\rho_\sigma(w)$ for the r=1 2CK pseudogap Anderson model both in equilibrium and non-equilibrium system, where the magnetic impurity symmetrically coupled to leads of Lorentzian bandwidth 2W and chemical potential μ_R and μ_R. Note that: in our study, we use D to replace W to be half-bandwidth. Here, all energy is units of Γ, the coupling constant of leads and dot, the half-bandwidth at half-maximum is $W = 100$ and temperature $T = 0.005$. The dashed cure represents out of equilibrium impurity DOS, Kondo peak splits into two suppressed peaks. The p-h symmetric impurity DOS is shown as the solid line, where single Kondo peak is at $w = 0$. Adapted from Ref. [57]. 37

2.5 The scaling is characteristic of a Fermi liquid when $(eV/K_BT_k)^2$ plot. The conductance does not follow a linear behavior, when $(eV/k_BT_k)^{0.5}$ plot. Therefore, rule out spurious effects in the real 2CK behavior for type "π" Co impurities on graphene. Adapted from [6]. 38

2.6 The quantum phase transition in graphene can be investigated by controlling the chemical potential μ_0. When $\mu = 0$, there is no 2CK state, always in LM state. If $\mu \neq 0$, the quantum phase transition between LM state and 2CK can be observed. Adapted from [41]. 39

2.7 (a) The phase diagram for 2CK-LM crossover QPT, parameter j represents coupling Γ or chemical potential μ, and j^* is the crossover scale for a fixed temperature $T_0 = 5 \times 10^{-7}D$. All parameters in units of half-bandwidth D=1, and T_k and T_0 are energy scales associated with the 2CK universal scaling. (b) A spin one half impurity couples symmetrically to the two sublattices of two graphene leads out of equilibrium, where two graphene leads are in thermal equilibrium, respectively. (c) Doped graphene in momentum space. Adapted from [60]. 40

2.8 The impurity DOS via NCA v.s. different chemical potential μ in units of D. Dirac point is located at $w/D = 0$, and Kondo peaks are pinned near each μ. Different levels w/D with different chemical potentials μ correspond to different Fermi levels, respectively. The parameter are $T_0 = 5 \times 10^{-}7$D, $\Gamma = 0.2D$, $\epsilon_d = -0.2D$, where D is half-bandwidth. T_0 is temperature of the system, Γ is coupling constant of leads and dot, and ϵ_d is dot level. Adapted from [60]. 42

2.9 (a) The linear conductance in equilibrium system. It show square root behavior at temperature which is lower than Kondo temperature. (b) There is an additional power law behavior at high temperature in equilibrium conductance scaling. It shows $T^* \sim |\Gamma - \Gamma^*|^{1/\mu}$, where $\Gamma^*$is a small number, 0.05D and $\mu \sim 0.1$. (c) Nonlinear conductance at $\Gamma = 0.2D$. The fixed parameters are $T_0 = 5 \times 10^{-7}D, \mu = -0.1D, \epsilon_d = -0.2D$, where $D = 1$ is half-bandwidth. (d) The $(eV/k_BT)^2$ behavior arises as $(eV/k_BT) << T$. (e) The $(eV/k_BT)^{\frac{1}{2}}$ behavior arises as (eV/k_BT) is between T and T_K. Adapted from [60]. 43

3.1 The phase diagram of equilibrium and non-equilibrium conductance. The phase diagrams delineated by T^* and V^*, which is crossover scale in equilibrium and out of equilibrium, respectively. The inverse of crossover scale is correlation length, ξ, which is diverge in quantum critical region, and $\nu_T = 4$, $\nu_V = 0.5$ are universal factor called as correlation length exponent. Due to ν_T, ν_V are different, the universal scaling in equilibrium is different from out if equilibrium. Here, critical point is at and near $r_c = 0.115$, even if G(0,T) and G(V,T) have slightly different parameters (Γ and ϵ_d). 45

3.2 The r=0.05 density of states of impurity non-equilibrium system with $\Gamma = 0.3D, \epsilon_d = -0.3D, T = T_0 = 5 \times 10^{-7}D$, where $D = 1$. The impurity DOS exhibits asymmetry graph, where no peak at $_d + U$ due to particle-hole asymmetry. The non-equilibrium density of states with bias, $V = 0.038D$, Kondo peak divided into two peaks, because the Fermi energy of left and right leads are different, the width between two peaks is equal to bias. . . 46

3.3 The Kondo peak of impurity spectral function with $\Gamma = 0.28D5, \epsilon_d = -0.2D$, and $T_0 = 5 \times 10^{-7}D$ by varying exponent r. (a) The full impurity DOS with p-h asymmetry. (b) Kondo peaks for different r in Fig.(3.3.a). . 48

3.4 The conductance v.s. T with varying r in equilibrium system , where $\mu = 0$, $\Gamma = 0.28D$, $\epsilon_d = -0.2D$ are fixed, and the half-bandwidth D=1. 49

3.5 To illustrate $G(0,T) - G(0,0) = B_k T^{\frac{1}{2}}$ scaling for $0 < r < 1$, but we can't get a reasonable result. The $\sqrt{T}$ behavior of differential conductance is obvious for small r, but it gradually disappears as r increase. Here, T_d is the non-universal factor, and $\mu = 0$, $\Gamma = 0.28D$, $\epsilon_d = -0.2D$, $D = 1$. 50

3.6 To illustrate σ_T v.s. $|r - r_c|$ plot with $\mu = 0$, $\Gamma = 0.28D$, $\epsilon_d = -0.2D$, where$D = 1$. 51

3.7 The universal scaling in G(0,T) is given by Eq.(3.1) with $\Gamma = 0.28D$, $\epsilon_d = -0.2D$ and $\mu = 0$, where$D = 1$. Set$r = 0.115$ is the critical point. . . . 52

3.8 Crossover scale T^* v.s. $r - r_c$ plot with $\Gamma = 0.28D$, $\epsilon_d = -0.2D$ and $\mu = 0$, where$D = 1$. 53

3.9 Non-equilibrium conductance of 2CK pseudogap Anderson model. G(V,T) saturates at a constant value for $V << T$, other parameters are $T = T_0 = 5 \times 10^{-7}D$, $\epsilon_d = -0.3D$ and $\Gamma = 0.3D$, $D = 1$. The bias voltage V is in unit of half-bandwidth D. 54

3.10 Scaling of non-equilibrium conductance, G(V,T) follows Eq.(2.53). The parameters are set as $T = T_0 = 5 \times 10^{-7}D$, $\epsilon_d = -0.3D$ and $\Gamma = 0.3D$, $D = 1$. The scaling exhibits the square root and square behavior of eV/k_BT, but reduced as exponent r increases. 55

3.11 σ_V v.s. $|r - r_c|$ plot with $\mu = 0$, $\Gamma = 0.3D$ and $\epsilon_d = -0.3D$. We set D=1. . 56

3.12 The non-equilibrium universal scaling in conductance for different r at low temperature, $T = 5 \times 10^{-7}D$. we set dot level $\epsilon_e = -0.3D$, $\Gamma = 0.3D$, and D=1. 56

3.13 Crossover scale V^* v.s. $|r - r_c|$ plot with $\mu = 0$, $\Gamma = 0.3D$ and $\epsilon_d = -0.3D$. We set D=1. 57

4.1 This figure depicts the equilibrium thermal transport and Fermi function. Red line represents $T \neq 0$ Fermi function, where particles may be excited by thermal energy. 60

4.2 The non-equilibrium transport in our system depends on current. The Fermi function for non-equilibrium case is different from the one in equilibrium because of the difference between chemical potential of the left and right leads. Fermi function of the left and right are different. The Fermi function of non-equilibrium system shows a jump $f_L - f_R$ across the impurity. 62

4.3 The three dimensional phase diagram to describe QPT between LM and 2CK both in equilibrium (G(0,T)) and out of equilibrium (G(V,T_0)). The quantum criticality can be accessed either by G(0,T) in equilibrium and or by G(V,T_0) out of equilibrium. The equilibrium and non-equilibrium conductance show distinct scalings at criticality. 63

Contents

1 Introduction **1**

1.1 Kondo Effect 1

1.1.1 Kondo Hamiltonian 3

1.2 Kondo Effect In Quantum Dot System 4

1.2.1 Coulomb Blockade Oscillations With Kondo Effect 5

1.3 Quantum Phase Transitions (QPT) 9

1.3.1 Two Channel Kondo (2CK) Physics 12

1.3.2 The Pseudogap Kondo Problems 16

2 Large N Approaches To 2CK Anderson Model **24**

2.1 Methods To N-fold Degenerate Anderson Model 25

2.1.1 The Foundation Of Slave Boson Representation 25

2.1.2 Non crossing approximation (NCA) approach 26

2.2 The 2CK Pseudogap Anderson Model out of equilibrium 27

2.3 Constant Density of States And Doped Graphene 36

2.3.1 Results Of Constant Density Of States Anderson Model 36

2.3.2 Results And Physics Of Doped Graphene 38

3 Results Of The 2CK Pseudogap Anderson Model: Quantum Phase Transition and Quantum Criticality **44**

3.1 Quantum Criticality Shows In Impurity Density Of States 45

3.2 Conductance near LM-2CK Quantum Critical Point 48

3.2.1 Equilibrium Conductance G(0.T) 49
3.2.2 Non-equilibrium Conductance G(V,T_0) 52

4 Summary And Conclusion **58**

Appendix **61**

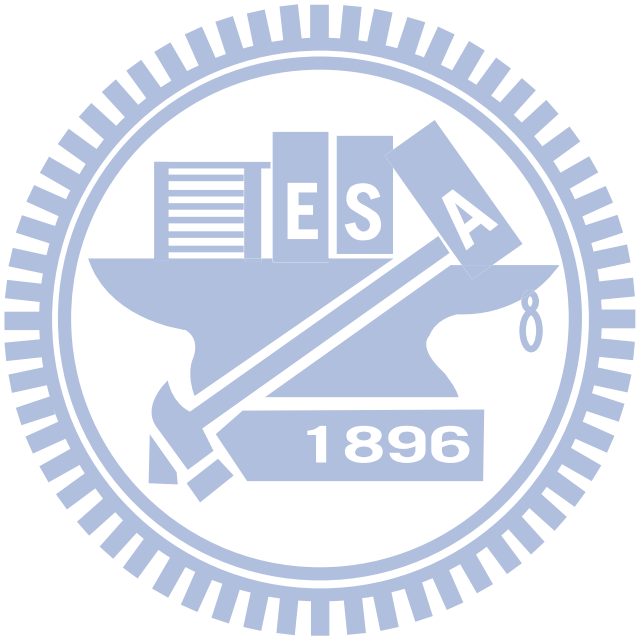

Chapter 1

Introduction

1.1 Kondo Effect

In 1930s, there was an important discovery in solid state physics, where the resistivity in some non-magnetic metals with magnetic impurities manifest itself a minimum at a certain temperature shown as Fig.(1.1.a). This important phenomenon was known as Kondo effect. There are many review papers, books, thesis and related information about Kondo effect [1, 2, 3, 4, 5, 6]. Due the advances in nano-technology, Kondo effect was applied in quantum dot systems, therefore Kondo effect shows different characteristic in bulk system compared to quantum dot (QD) system. The conductance in a QD system as shown in Fig.(1.1.b). We will illustrate the phenomenon of the Kondo effect in bulk system below [1, 5, 7], then introduce Kondo effect in QD system in Section 1.1.2.

The original Kondo phenomenon cannot be explained by the scattering theory between electron and phonon. J.Kondo successfully explained this phenomenon in 1964 by spin-flip scattering as shown in Fig.(1.2) [8]. Theoretically, a magnetic impurity is screened by the spin of nearby conduction electrons, leading to a spin singlet, so-called Kondo singlet. The Kondo singlet appears when $T < T_k$, T_k is defined as Kondo temperature. The size of Kondo cloud made of conduction electrons defined as $\xi_k^0 \sim \frac{h\nu_F}{k_B T_k}$, where ν_F is Fermi velocity. The larger Kondo cloud implies a weaker Kondo coupling. Alternatively,

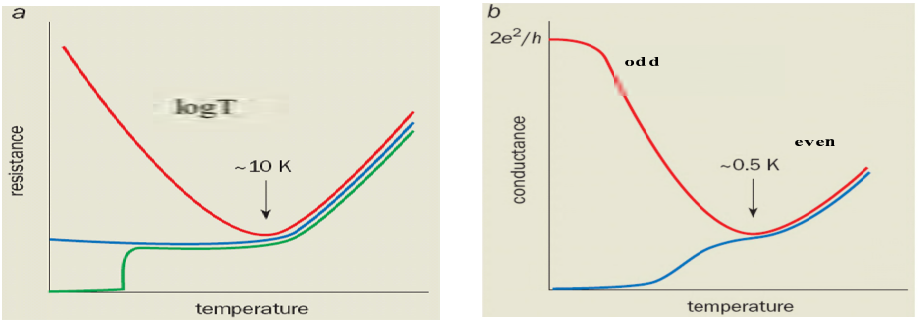

Figure 1.1: (a) Redline shows resistivity in metals contained magnetic impurities: at low temperature, using third order perturbation theory, Kondo found that this scattering process leads to a lnT behavior in resistivity. Blueline shows resistivity in normal metals. (b) In quantum dot system, Coulomb blockade influence conductance. At low temperature, when temperature decreases, conductance increases (decreases) if electron number is odd (even). Kondo effect appears only odd number, Kondo effect leads to conductance increased at low temperature in QD system. Adapted from [1, 7].

Kondo effect can be conveniently described by the s-d model proposed by Zener [9], where magnetic moments carry spin S_d coupling to conduction electrons via $Js \cdot S_d$, where the exchange interaction J was called as Kondo coupling ($J > 0$), S_d is the impurity spin, and s is spin of conduction electrons. The s-d model can be related to Anderson model at certain parameters regime, presented by P.W. Anderson [5, 6, 11]. Coqblin-Schrieffer transformation can transform Anderson model to Coqblin-Schrieffer model, also called as Kondo model [5, 10, 12]. Note that perturbation theory used to explain Kondo effect only for $T > T_K$. It breaks down for $T < T_K$, one needs Numerical Renormalization Group (NRG) to resolve this issue. More theoretical calculations will be introduced in this chapter.

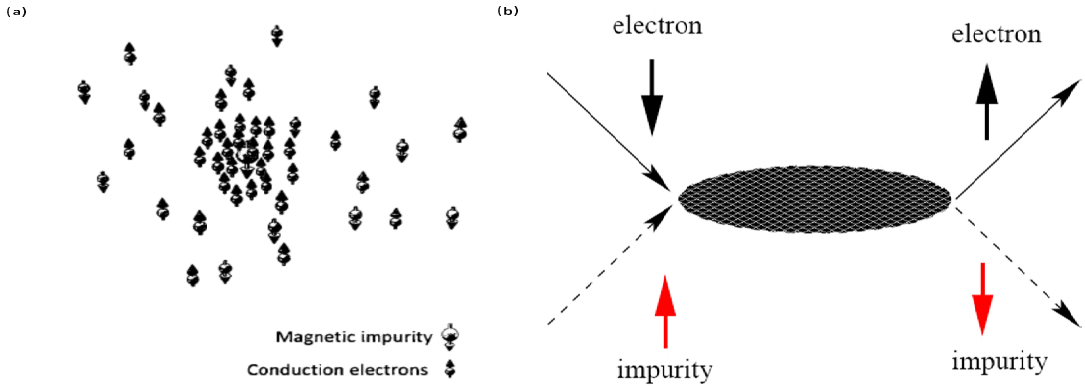

Figure 1.2: (a) Kondo effect happened because of impurity screened by spin one half of electrons. Adapted from [58]. (b) Electron-impurity spin-flip scattering.

1.1.1 Kondo Hamiltonian

From previous section, we know that the magnetic moment of impurity is screened by conduction electrons, leading to Kondo effect. In this section, we provide a mathematical description of the Kondo effect. We start from a single impurity $S = \frac{1}{2}$ Anderson Hamiltonian [5, 6].

$$H = \sum_{\sigma} \epsilon_d d_\sigma^\dagger d_\sigma + \sum_{k\sigma} \epsilon(k) c_{k\sigma}^\dagger c_{k\sigma} + U n_\uparrow n_\downarrow + \sum_{k\sigma} (V_{k\sigma} d_\sigma^\dagger c_{k\sigma} + H.C.) \tag{1.1}$$

The first term in Eq.(1.1) describes the local moment state of impurity with energy ϵ_d, where σ is the spin index. The second term describes conduction electrons, where k is the momentum space of Fermi sea. The third and fourth term are the on-site Coulomb repulsion and the hopping between the leads and the dot. The Coulomb repulsion potential U is the energy cost for the localized state occupied by two electrons (of opposite spins). From Anderson model, If $\epsilon_d < \epsilon_F$ (which is the Fermi energy of the metal) and $\epsilon_d + U > \epsilon_F$, the single occupied site will have a net spin-1/2. By using Coqblin-Schrieffer transformation, Anderson model Hamiltonian can be mapped onto the Kondo Hamiltonian in $U >> V$ regime [5, 12]:

$$H \simeq \sum_{k\sigma} \epsilon(k) c_{k\sigma}^\dagger c_{k\sigma} + \sum_{k,k'} J_{kk'} s_{kk'} \cdot S_d, \tag{1.2}$$

where $J_{k,k'}$ represents the anti-ferromagnetic coupling which is given by:

$$J_{kk'} = V_{k\sigma}V^*_{k'\sigma}[\frac{1}{\epsilon_d - \epsilon_k + U} + \frac{1}{\epsilon'_k - \epsilon_d}], \tag{1.3}$$

where ϵ_k is energy level of conduction electrons, ϵ_d is energy level of quantum dot, $s_{kk'}$ is the spin of conduction electrons, and S_d is an impurity spin. Because the Kondo resonance lies exactly at the Fermi energy, the contribution of exchange process is only from states around Fermi energy(ϵ_F). So we set that $\overline{\epsilon_d} \equiv \epsilon_d - \epsilon_F$, $\overline{\epsilon_k} \equiv \epsilon_k - \epsilon_F$ and $\overline{\epsilon_k} \sim 0$. Since $\overline{\epsilon_d} < 0$ and the Coulomb potential U is larger than $\overline{\epsilon_d}$, $J_{kk'}(\sim J_{k_Fk_F})$ is the anti-ferromagnetic coupling($J_{kk'} > 0$). For $U >> |\overline{\epsilon_d}|$, the expression reduces to:

$$J_{k_Fk_F} \equiv J \sim -\frac{|V^2_{k\sigma}|}{\overline{\epsilon_d}} = \frac{|V^2_{k\sigma}|}{\epsilon_d - \epsilon_{k_F}} > 0. \tag{1.4}$$

The second term of Eq.(1.2) is precisely the s-d interaction term written as $H_{ex} = J(r) \cdot S$. It describes the spin exchange between an impurity and the surrounding conduction electrons. The distance r is measured from the impurity site to conduction electrons. This simple model explains the Kondo problem that resistivity of metals in magnetic impurity bulk system at low temperature will increase logarithmically. We will discuss Kondo effect in QD system in Section 1.1.2 and two-channel Kondo in Section 1.1.4.

1.2 Kondo Effect In Quantum Dot System

Due to the progress of science and technology, scientist can fabricate semiconductor structure under nano-mater scale. The advance of micro-fabrication and cooling technology make a chance that we can research Kondo effect in nano-size system. Kondo physics can be realized in a tunable quantum dot (TQD). TQD is made by the single electron tunneling transistor (SET) with two dimensional electron gas (2DEG) heterostructure, as shown in Fig.(1.3) [1, 18, 21]. SET device has GaAs/AlGaAs layer and multiple electrodes, where three gate electrodes on left and the other one on right in the picture. Then GaAs layer confines 2DEG repelled by electrodes, and induces two tunneling junctions under and above it. A metallic island is confined between two tunneling junctions called "quantum dot (QD)". One of early experiments of Kondo effect in QD system was

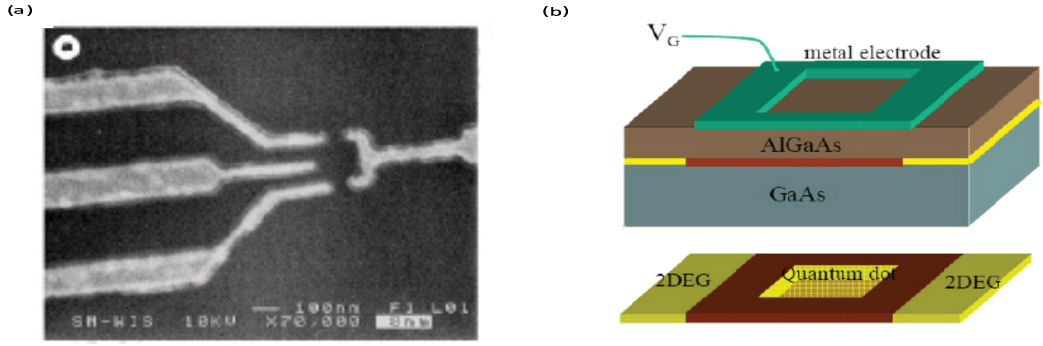

Figure 1.3: (a) Scanning electron micrograph of SET device. The top and down electrodes on the left side and the electrode on the right side are used to operate the barrier of quantum dot. The middle electrode on the left side are used to tune the energy level of QD relative to 2DEG [13, 14]. (b) Schematic SET device [21].

made by D. Gordhrber-Golen et.al in 1998 [13, 14, 17]. The conductance in QD systems is quantized by Coulomb blockade (CB) oscillations, leading to the difference of Kondo effect between QD systems and bulk systems.

1.2.1 Coulomb Blockade Oscillations With Kondo Effect

The original Kondo physics (in bulk system) was introduced in last section, where Kondo effect induce resistivity to be enhanced. This section, we will discuss the Kondo effect in QD system, which is very different from bulk system. In the single electron tunneling transistor (SET) device, the Coulomb blockade (CB) oscillations affects the conductivity [21, 22] as shown in Fig.(1.4). In Fig.(1.4.a), it exhibits conductance increasing as odd number in quantum dot (blue line), and there are peaks at $V_{SD} = 0$ in Fig.(1.4.b). The peaks at $V_{SD} = 0$ are temperature dependent, as temperature is lower, peak is higher. These peaks are due to Kondo effect, so-call Kondo peaks. We will introduce CB and and briefly discuss the results in theory and experiment, then discuss Kondo effect in SET.

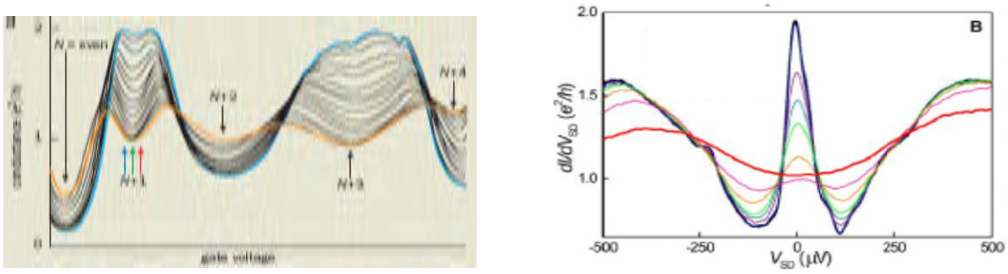

Figure 1.4: (a) Conductance has two different behaviors at even and odd electron number. (b) The zero bias differential conductance anomaly at $V_{SD} \sim 0$, where V_{SD} is the voltage difference between source and drain. [1, 13, 14].

Coulomb Blockade

Coulomb blockade oscillation appears due to strong Coulomb potential system, that's why it called as Coulomb blockade. In the SET device, Coulomb potential affect the electron tunneling between leads and dot, illustrated in Fig.(1.5). The first order tunneling is blocked by the Coulomb blockade, where U is Coulomb potential between the electron of quantum dot and lead. The CB Hamiltonian related to constant interaction model was constructed as [21, 22]:

$$H_D^{CB} = \sum_{\mu} \xi_\mu c_\mu^\dagger c_\mu + E(N), \quad E(N) = E_C N^2 - eV_g N \tag{1.5}$$

, where E(N) is the interaction term of the system, including gate voltage term as eV_gN, where gate voltage leads to a electric field that increases the energy of dot electrons. In general, we have to simultaneously think about source, drain, and gate voltage. Here we lump all terms in a gate voltage term. The energy $E_c = \frac{e^2}{2C}$, where C is the capacitance of a single electron. The bias voltage leads to $\mu_L \geq \mu_{dot} \geq \mu_R$, and the bias voltage difference between the left lead (source) and the right lead (drain) was defined as V_{SD}. Because of the inequality of chemical potential, electrons can flow, therefore an added electron from source excites dot energy from $E_{dot}(N-1)$ to $E_{dot}(N)$, then an electron hops from dot to

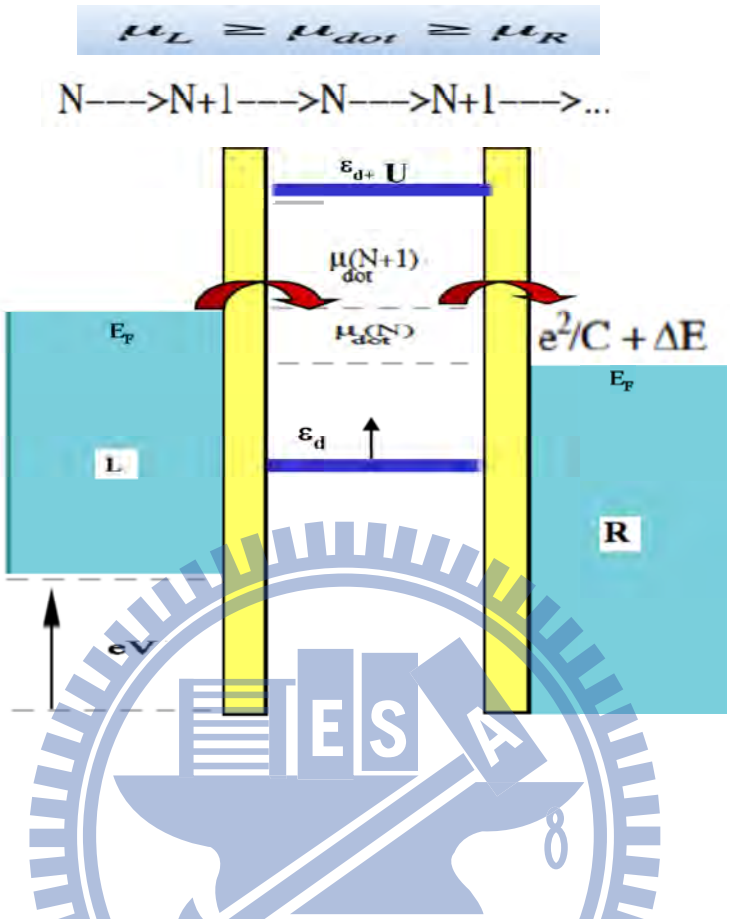

Figure 1.5: The illustration of Coulomb blockade. The first order tunneling is blocked by Coulomb potential U, the cotunneling (2nd) solution is solvable. The additional energy for N to $N+1$ state is $E^2/C + \Delta E$. The voltage spacing between source and drain is defined as V_{SD} which is eV here.

drain, leading dot energy from $E_{dot}(N)$ to $E_{dot}(N-1)$. The tunneling occurs when

$$\alpha e V_g(N) = E(N+1) - E(N), \tag{1.6}$$

where $\alpha = C_g/C$is the ratio of gate capacitance to total capacitance, called "gate coupling". The $\alpha e V_g(N)$ is similar to chemical potential of quantum dot, which is

$$eV_g(N) \equiv \mu_{dot}(N) = E_{dot}(N) - E_{dot}(N-1) = (n - \frac{1}{2})\frac{e^2}{C} - eV_g + E_N, \tag{1.7}$$

the remain terms defined as E_N. The additional energy is given by $\Delta\mu_{dot}$, where

$$\Delta\mu_{dot} \equiv \mu_{dot}(N) - \mu_{dot}(N-1) = \frac{e^2}{C} + E_N - E_{N-1} = \frac{e^2}{C} - \Delta E. \tag{1.8}$$

The irregular spacing of the single electron levels is defined as ΔE. When charging energy $\frac{e^2}{C}$ is much larger than ΔE, CB oscillations is dependent on it. The peak spacing of CB as a function of gate voltage is given by

$$\Delta V_g = \Delta\mu(N)/e\alpha = (e/c^2 + \Delta E)/e\alpha, \tag{1.9}$$

while condition Eq.(1.6) gives the gate voltage of N-th Coulomb peak. We take differential of E(N) in Eq.(1.5) with respect N, we obtain the optimum number of particles,

$$N_{opt} = eV_g/2E_c \tag{1.10}$$

When optimum number is

- Integer: There is an energy gap for adding electrons.
- Half-integer: There are two degenerate charge states, then electrons can transit.

As shown in Fig.(1.4.a), it exhibits difference results indicated different number of electron on quantum dot, and Fig.(1.4.b) exhibits non-equilibrium differential conductance with anomaly behavior at $V_SD \sim 0$ [1]. The electron number can be changed by gate tuning. The CB oscillation affect the conductance by electron number, then we discuss how Kondo effect can overcome CB in QD.

Kondo Effect In Quantum Dot System

The tunable QD is sometimes similar to individual artificial magnetic impurity, which leads to Kondo screening for $(T < T_k)$. When optimum number is odd, the QD with a single electron which is occupying the top-most quantum state, which is similar to a magnetic impurity. In other words, Kondo screening occurs with a single spin-degenerate energy state ϵ_d, no Kondo effect when optimum number is even. Kondo effect appears when $(T < T_k)$, where the Kondo temperature T_k found to be:

$$T_K = [U\Gamma]^{\frac{1}{2}} e^{\frac{-\pi(\mu-\epsilon_d)}{2\Gamma}}, \tag{1.11}$$

where (ϵ_d) is dot level, (Γ) is a coupling between leads and dot, and chemical potential μ [5]. These parameters all influence Kondo temperature. The Kondo effect is

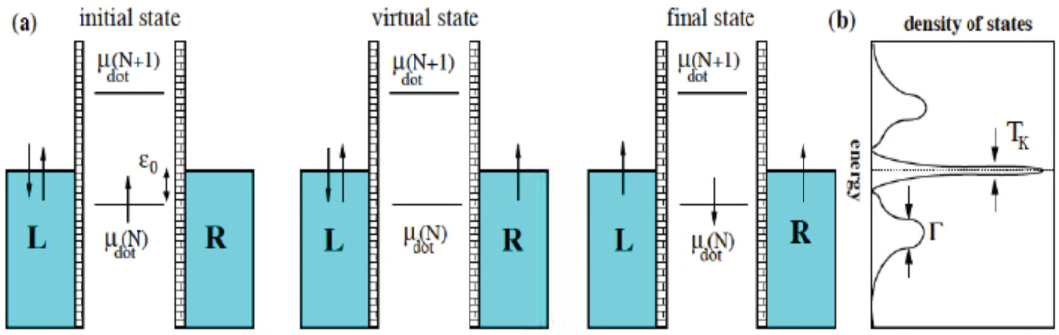

Figure 1.6: (a) Spin-flip cotunneling process of Kondo effect. (b) The density of states(DOS) of quantum dot, The Kondo resonance lies at the Fermi energy, Kondo effect occurs when the temperature is below the Kondo temperature T_k. Adapted from [21].

illustrated in Fig.(1.6), the first order tunneling is blocked by the Coulomb blockade, second order tunneling (cotunneling) leads to Kondo screening with spin-flip exchange. A narrow-resonance is seen in the density-of-states (DOS) of the QD. In summary, the system with tunable tunnel coupling to the leads, there is CB oscillation affected conductivity by electron number when $T > T_k$. When $T < T_k$, we have to think about the coupling between Kondo effect and Coulomb blockade. The odd electron number on the dot provides a single spin-degenerate state ϵ_d, which is a single electron with spin up or down. This condition leads to Kondo screening with spin-flip exchange, and enhanced conductance. The conductance of Kondo effect in QD system with even and odd number is shown in Fig.(1.1.b).

1.3 Quantum Phase Transitions (QPT)

Quantum phase transition (QPT) are the continuous phase transition of ground states at $T = 0$ by tuning the sets of the system parameters in Hamilton [36]. The energy level

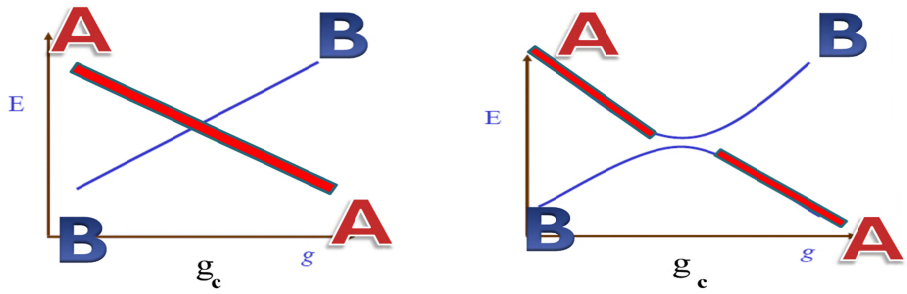

Figure 1.7: (a) The first order phase transition. Though g_c, the ground state becomes B state from A state with level crossing. (b) The higher order phase transition, avoiding level crossing. The phase transition whose ground state is form A state to B state as g exceeds g_c is a continuous process. Ref. [36]

diagrams as a function parameter g are shown in Fig.(1.7). H(g)=H_0+gH_1, where H_0 and H_1 commute to each other, and g is the coupling constant. As shown in Fig.(1.7.a), ground state is state A when the coupling g is below g_c, but it becomes state B when $g > g_c$, where g_c is the critical point of the coupling g. This is the first order phase transition, which is a level crossing. Fig.(1.7.b) shows the 2nd order phase transition, which is a continuous phase transition from $g < g_c$ to $g > g_c$, avoiding level crossing. QPT is the phase transition as shown in Fig.(1.7.b), continuous process and without level crossing at zero temperature. The quantum critical behaviors of QPT systems exhibit divergence in correlation length $\xi \sim |g - g_c|^{-\nu}$. Here, the correlation length exponent ν is a universal factor. This leads to universal power-law scaling behaviors in all thermal dynamical observable. These behaviors in quantum critical regime cannot be described in Fermi liquid theory, so called "non-Fermi liquid" behaviors. Quantum critical phenomenon is an important subject in condensed matter as they provided universal behaviors at the quantum critical point (QCP). Single impurity Kondo problems have been well-known, we investigate Kondo effect break down for adding other competition ground state in the

system at $T \to 0$, it leads to QPT and quantum critical phenomenon. Examples for QPT in Kondo system: include the double quantum dots (DQD) system leads to a quantum phase transition between Kondo effect and spin-singlet, two-channel Kondo ground state, and pseudogap Kondo problems, as we will introduce below. In this thesis, we investigate QPT for 2CK pseudogap single impurity Anderson model, the pseudogap Kondo problem and two-channel Kondo physics will be briefly introduced in below subsections. Here, we discuss DQD problem for understanding QPT in Kondo system.

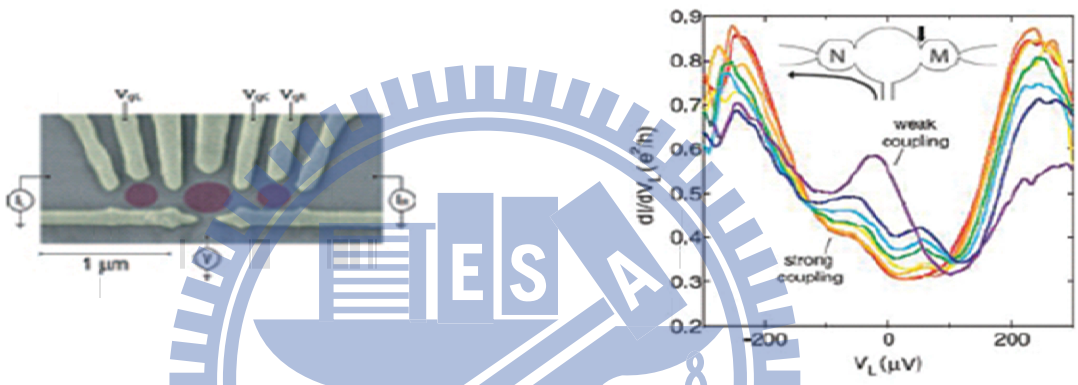

Figure 1.8: (a) The diagram is obtained via the scanning electronic micrograph (STM) in experiment of N. J. Craig *et. al.* [37]. (b) Conductance of left quantum dot. When odd number of electrons on the quantum dot and RKKY anti-ferromagnetic interaction is stronger than Kondo coupling, Kondo effect will be suppressed by RKKY. Adapted from [37].

The double quantum dot experiment made by N. J. Craig *et. al.* [37] for understanding quantum phase transition is shown in Fig.(1.8). The device in Fig.(1.8.a) shows two quantum dots coupled through an open conducting region, which provides exchange coupling between two dots. The gate voltage V_{gL} (V_{gR}) changes the occupation number and energy of left (right) dot, and the coupling between the right QD and central region can be tuned by gate voltage V_gC. The result is shown in Fig.(1.8.b) that odd number

of electrons on both dots leads to split zero bias Kondo resonance into two peaks. If the occupation number of one of QD is even, there is no zero bias Kondo resonance. Theoretically, this double QD Kondo problem was studied via the numerical renormalization group (NRG) [39, 40] and conformal field theory [32, 54], which is relevant for experimental in Ref. [37]. The quantum critical diagram of double quantum dots system is shown in Fig.(1.9). Kondo effect can be observed in double QD system as RKKY coupling K is small. But Kondo effect can be suppressed if RKKY coupling exceeds the critical point K_c. In this case, two quantum dots are coupled anti-ferromagnetically through an open conduction region via RKKY effect, inducing a local spin singlet between two spins on the dots ground state. A quantum critical point located at $K{=}K_c$ separate Kondo from local spin-singlet phase. The universal power-law scaling behaviors were identified in quantum critical region.

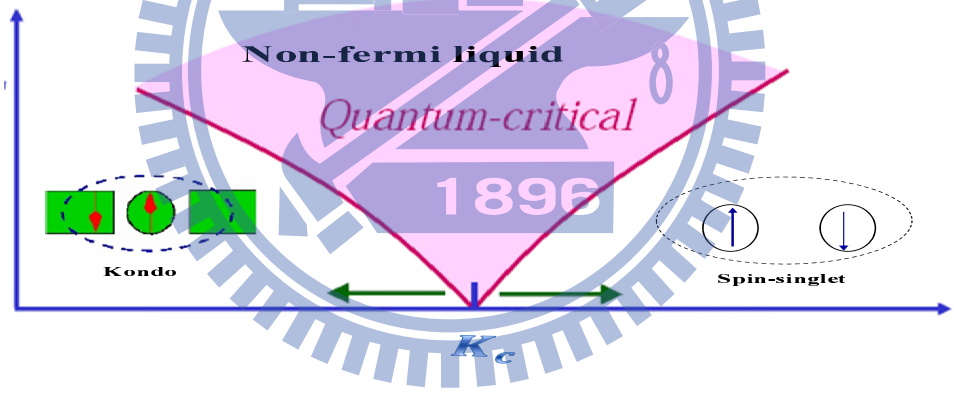

Figure 1.9: The quantum phase transition coupling K is RKKY coupling, and quantum critical point (QCP) with criticality at zero temperature is located at the K_c. Adapted from [39].

1.3.1 Two Channel Kondo (2CK) Physics

We have introduced Kondo effect in single channel QD system in Section 1.2 and 1.3. Here, two independent electron reservoirs are applied to QD system, it leads to two-

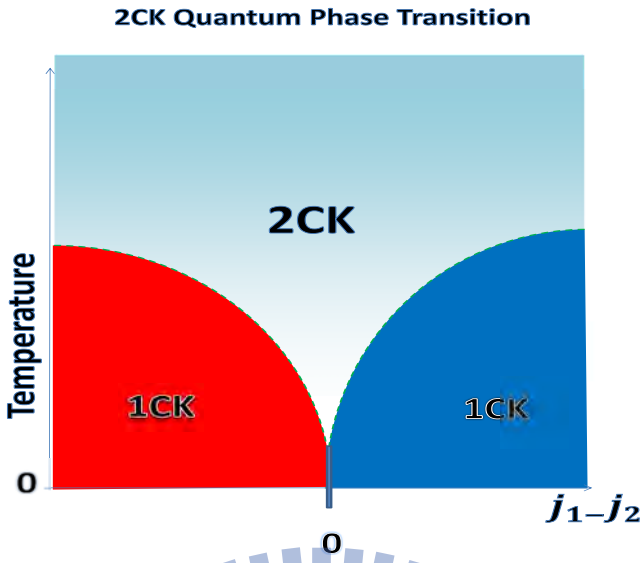

Figure 1.10: Quantum phase transition diagram of two-channel Kondo, where $H_{2CK} \sim J_1 S_1(r) \cdot S + J_2 S_2(r) \cdot S$, and J_1, J_2 are Kondo coupling of each channel, respectively. Blue and red phase correspond to blue and red channel in Fig.(1.11), and J_1 (J_2) is the Kondo coupling of red (blue) channel. At zero temperature, one can obtain 2CK state for symmetric coupling. There is still the 2CK state if coupling are some imbalance at finite temperature. The quantum critical region exhibits 2CK non-Fermi liquid behavior at finite temperature. [38]

channel Kondo (2CK) effect. Two-channel Kondo model was introduced by Zawadowski and Nozi‘eres *et. al.* decades ago, where a local spin S is coupled to two independent electron reservoirs [19, 20, 23, 6]. The discussion for 2CK details in theory is in Appendix A. Two independent electron reservoirs all couple to single QD system has been realized in recently years [16]. Compare to single channel Kondo Hamiltonian Eq.(1.2), the 2CK Hamiltonian can be written as

$$H_{2CK} \sim J_1 S_1(r) \cdot S + J_2 S_2(r) \cdot S. \tag{1.12}$$

The $S_1(r)$ and $S_2(r)$ is a conduction electron spin of each independent channel. The coupling J_1 and J_2 of Eq.(1.6) represents anti-ferromagnetic coupling of each independent channel, respectively, where each reservoir individually attempts to screen the local spin. The competition between J_1 and J_2 leads to continuous phase transition of two competition single channel ground states at zero temperature. The quantum critical region of two competition single channel QPT is as 2CK fixed point and it exhibits non-Fermi liquid (NFL) behavior as shown in Fig.(1.10). In a symmetric case, the Kondo couplings J_1 and J_2 are equally coupled to the magnetic impurity at zero temperature, leading to 2CK ground state [34]. If $J_1 \neq J_2$ at zero temperature, the localized impurity spin couples to one of the electron channel, resulting in single channel Kondo effect (1CK). However, we can observe 2CK effect at finite temperature even if $J_1 \neq J_2$, the condition is that the Kondo coupling asymmetry have to be small enough [6]. At finite temperature, we can investigate quantum critical region at 2CK fixed point and find universal scaling [38, 6]. Landau Fermi liquid theory is a theoretical model of interacting fermions describes properties of general metals at low temperature. The behavior in 2CK quantum critical region can be not be explained under Fermi liquid theory, so called non-Fermi liquid (NFL) behavior. NFL behavior appear in heavy fermion materials. Some heavy fermion materials show specific heat anomalies [24, 25, 26, 27]. The specific heat in heavy fermion metals [3, 32, 33]and anomalous shrinkage of zero-bias conductance [30, 31] in 2CK system have been observed. The entropy of impurity spin in 2CK system is anomaly at $T \to 0$, the entropy of impurity can be written as

$$S = k_B ln(\Omega), \tag{1.13}$$

Ω is number of states at $T \to 0$. We find 2CK entropy is $S = k_B ln(\sqrt{2})$, however, $\Omega = 2$ as $T \to 0$. Theoretically, the anomaly corresponds a free "Majorana fermion", which is the anti-particle of itself, two Majorana fermions is a complete fermion. Note that: $S = k_B ln(2)$ at $T \to 0$ for 1CK.

In experiments, it's difficult to control 2CK fixed-point stability. One needs fine control of each droplet in electrochemical potential, which can be adjusted near the voltage on the gate electrode [24]. The 2CK experiment was made by Potok and Goldhaber-Gorden

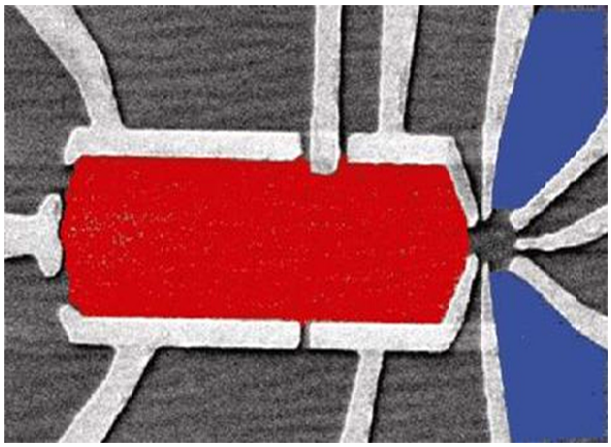

Figure 1.11: Two independent electron reservoirs couple to a QD in SET device. Two blue leads and a finite red reservoir represent two independent channel, respectively. Here, red reservoir has to be much large than QD, therefore, there are sufficient electrons to compose a conduction electron band. Two blue leads comes a reservoir which is faraway from QD. Adapted from [16].

et. al. [16], where the modified single-electron tunneling transistor (SET) with two spatially-separated sets of confined electrons can help us to understand 2CK on quantum dots. The SET device with two independent electron reservoirs is shown in Fig.(1.11). For avoiding one of electron reservoirs is scattering to the other, the red channel is hold zero conductance at low temperature, on the other hand, blue channel is hold finite conductance. There is a experimental scaling analysis can distinguish conductance behavior between 1CK and 2CK as shown in Fig.(1.12), where the experimental results for 2CK out of equilibrium system in conductance scaling.

The single-channel Kondo effect shows T^2, $(eV/k_BT)^2$ behavior at $T < T_K$, theoretically, it is Fermi liquid with scattering rate that varies as T^2. But the 2CK data in 1CK scaling deviates from $(eV/k_BT)^2$. However, the non-Fermi liquid as 2CK fixed shows $(eV/k_BT)^{1/2}$ behavior at $T < T_K$. In Fig.(1.12), 2CK universal scaling exhibits

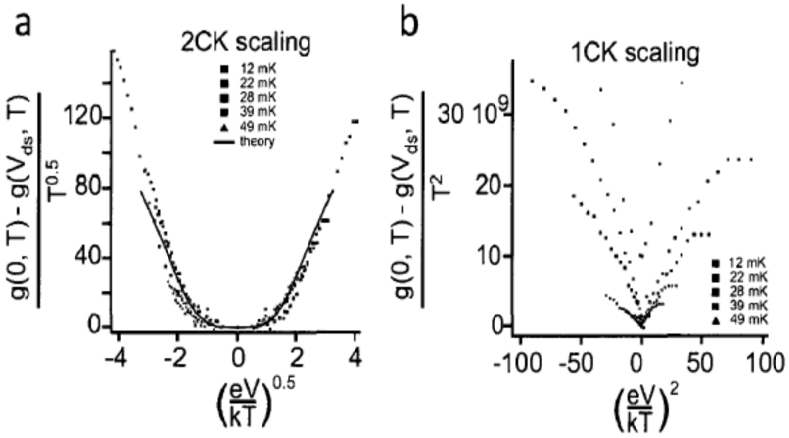

Figure 1.12: 2CK conductance data in 2CK and 1CK scaling, where 1CK scaling follows Fermi liquid $(eV/k_BT)^2$ behavior. 2CK universal scaling follows $(eV/k_BT)^{1/2}$ behavior, not Fermi liquid $(eV/k_BT)^2$, so-called NFL behavior. Adapted from [6, 38].

$(\sqrt{eV/k_BT})$ behavior. Theoretically, 2CK universal scaling in conductance can be analyzed by field theory, which will be discussed in Chapter 2, and summarized in chapter 4. In theory, 2CK can be extended to multi channel Kondo (M-channel) ($M \geq 2$) with non-trivial solutions [29, 28]. The large N approaches which are feasible theoretically used to solve the multi-channel Kondo problems. The large N approaches will be introduced in section 1.5 and Chapter 2.

1.3.2 The Pseudogap Kondo Problems

Here we define the pseudogap kondo problems. These are special Kondo problems where conduction electron density of states (DOS) vanishes in a power law fashion at $\omega = 0$ ($\rho_c(w) \sim |w|^r$, $0 \leq r \leq 1$). Pseudogap Kondo problems have been extensively studied in recent years, by RG, NRG [41, 43, 44, 45, 46, 47] ,and slave-boson large N technique [48, 61]. By tuning the exponent r of the pseudogap DOS, ground state of pseudogap

Kondo systems may undergo a QPT between Kondo and local moment (LM) state. If exponent r is too large, the conduction DOS is not sufficient to Kondo screening, leading to LM ground state. On the other hand, Kondo screening was observed at $T < T_K$ if the exponent r is small enough that conduction electrons are sufficient to screen the impurity. Pseudogap DOS in single channel and two-channel Kondo systems leads to QPT with particle-hole symmetry and asymmetry. The QPT in pseudogap Kondo can be analyzed by renormalization group (RG) techniques. We briefly introduce the rich ground phase diagrams of pseudogap Kondo system given by Matthias Vojta *et. al.* via perturbative RG and numerical renormalization group (NRG) approach [41, 43, 44].

Renormalization Group And Numerical Renormalization Group

Renormalization group (RG) approach originally comes from quantum field theory, and has been applied to condensed matter system. Anderson *et. al.* applied so called "poor man scaling RG" to Kondo problem [49], where all the leading to logarithmic terms were summed up via perturbation theory. However, perturbation theory breaks down for $T < T_K$ as the system reaches the strong coupling Kondo ground state. K.G. Wilson use a non-perturbative technique: numerical renormalization group (NRG) approach to analyze Kondo physics at $T < T_k$ [50, 51, 52]. There is the other non-perturbative method called Bethe ansatz, confirming Wilson's NRG calculation [53]. The s-d model was given a definitive result for ground state by NRG calculation. In condensed matter system, NRG can accurately describe magnetic doped metals , while methods can not. The QPT of pseudogap Kondo problems can be studied by using perturbative RG and NRG approach.

RG phase diagrams for 1CK single impurity pseudogap Anderson model

In results by Matthisa Vojta *et. al.* [41, 43, 44]. Pseudogap Kondo problems analyzed by perturbative RG leads to non-trivial fixed point and associated phase transitions. Here, we introduce the single impurity Anderson model coupled to single channel electron reservoir with particle-hole symmetry and asymmetry. We briefly introduce particle-hole symmetry and asymmetry below. The full symmetry of 1CK single impurity pseudogap

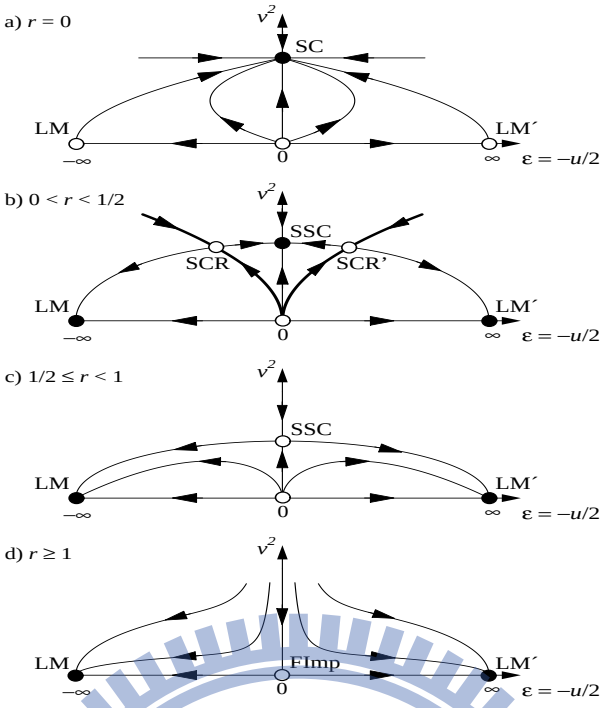

Figure 1.13: The RG flow phase diagram of particle-hole symmetric single impurity pseudogap Anderson model. The details are in text. Adapted from [43].

Anderson model with particle-hole symmetry is $SU(2)_{spin} \times SU(2)_{charge}$, where particle-hole symmetry is $SU(2)$ pseudospin symmetry. The 1CK single impurity Anderson model as Eq.(1.1) is coupled to pseudogap conduction electron density of states,

$$H = \sum_{\sigma} \epsilon_d d_\sigma^\dagger d_\sigma + \int_{-\Lambda}^{\Lambda} dk |k|^r k c_{k\sigma}^\dagger c_{k\sigma} + U n_\uparrow n_\downarrow + \sum_{k\sigma} (V_{kd} d_\sigma^\dagger c_{k\sigma} + H.C.). \tag{1.14}$$

The second term of in Eq.(1.1) was replaced by the bath Hamiltonian of pseudogap host conduction electron DOS. The other terms of Eq.(1.14) are the same as Eq.(1.1). The Λ is the untraviolet (UV) cutoff. In the presence of particle-hole symmetry, the Coulomb potential is assumed as $U_0 = -2\epsilon_d$. And the Hamiltonian is invariant by below transformation,

$$d_\sigma^\dagger \longrightarrow d_\sigma,$$

$$c_{k\sigma}^\dagger \longrightarrow c_{-k\sigma}.$$

On the other hand, if $U_0 \neq -2\epsilon_d$, the particle-hole symmetry is broken. For example, strong Coulomb potential leads to particle-hole asymmetry. From NRG calculations, the

fixed-point structure changes at r^* and $r = 1/2$, the relevant case of r=1 case is inaccessible from weak coupling. [43, 45] $r^* = 0.375$ is given by NRG. P-h symmetry is restored for $0 < r < r^*$. The RG flows of the particle-hole symmetric 1CK single impurity pseudogap Anderson model is shown in Fig.(1.13). The horizontal axis denotes the renormalized dot level ϵ, where $U = -2\epsilon$; the vertical axis is the renormalized hybridization V, hoping of dot and leads. The continuous boundary phase transitions were represented by the thick lines; the full (open) circles are stable (unstable) fixed points. Now, we introduce the fixed points corresponded to the phases,

LM : local moment ground state,

SC : strong coupling as Kondo-screened fixed point,

SSC : symmetric strong coupling fixed point,

SCR : symmetry critical region fixed point,

FImp : free impurity fixed point.

When r=0, the flow is towards to SC fixed point at any finite U. For $0 < r < 1/2$ case, LM fixed points are stable, the SSC fixed point which is stable is located at $\epsilon = 0$, and SCR (SCR') fixed point control the phase transition between SSC and LM (LM'). The SSC fixed point becomes unstable as $\leq r < 1$, and SCR (SCR') fixed point disappears. The phase transition between LM and LM' is controlled by SSC fixed point. When $r \geq 1$, there is no QPT. The first order phase transition with level crossing between LM and LM'. The FImp fixed point is located $U = 0$, meaning that no hoping between leads and dot. As particle-hole asymmetric 1CK single impurity pseudogap Anderson model: The RG flow phase diagram was shown in Fig.(1.14). Particle-hole asymmetric Anderson model can be realized as Coulomb potential is too large, where $U_0 \longrightarrow \infty$. The horizontal axis denotes the on-site dot energy levelϵ; the vertical axis is the fermionic coupling v. The bare on-site repulsion is fixed at $u_0 = \infty$. Here, we introduce the fixed points corresponded to the phases,

LM : local moment ground state,

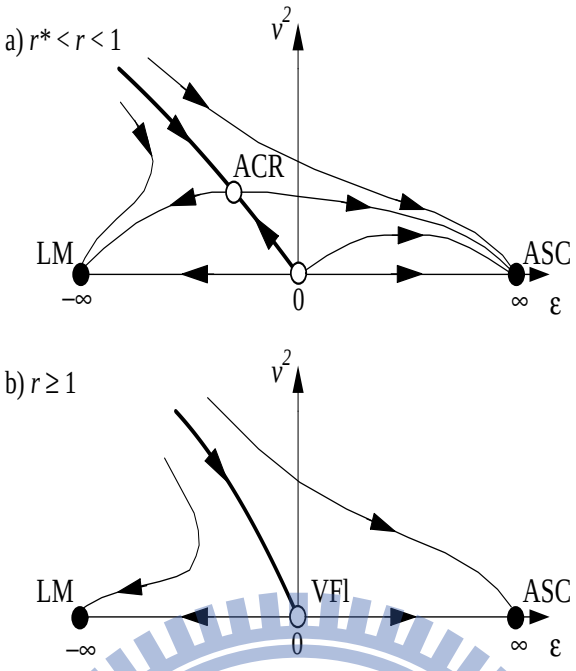

Figure 1.14: The RG flow phase diagram of particle-hole asymmetric single impurity pseudogap Anderson model. The details are in text. Adapted from [43].

ASC : asymmetry strong coupling fixed point,

ACR : asymmetry critical region fixed point,

VFI : the valence fluctuation fixed point.

The hybridization V_0 which is small leaves the moment unscreened, whereas large V_0 directs the flow towards ASC fixed point. When r=0, the constant DOS, where the strong-coupling fixed point is the same as in the p-h symmetric situation. For $0 < r < r*$ case, particle-hole symmetry is restored. The phase transition is controlled by ACR unstable fixed point as $r^* < r < 1$. When $r \geq 1$, there is no QPT. The first order phase transition with level crossing controlled by VFL. The VFI fixed point is located at $\epsilon = U = 0$.

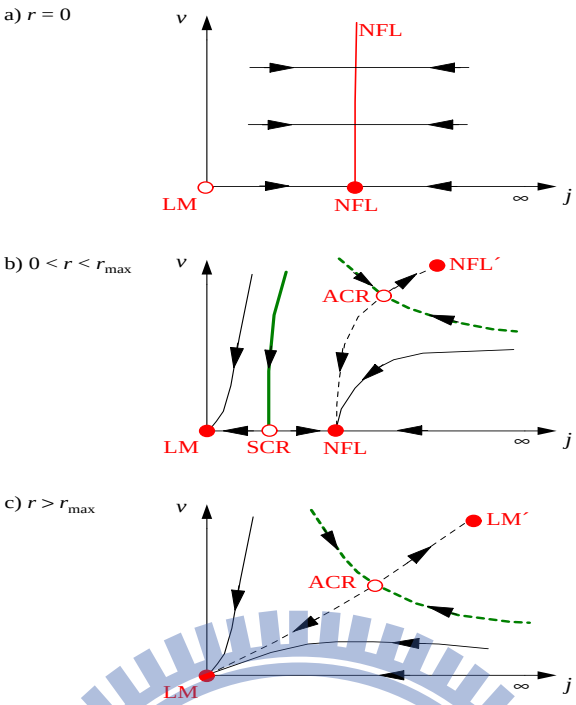

Figure 1.15: The RG flow phase diagram of 2CK particle-hole asymmetric single impurity pseudogap Anderson model. The details are in text. Adapted from [44].

RG phase diagrams for 2CK single impurity pseudogap Anderson and Kondo model

In the results of Matthisa Vojta *et. al.* [41, 43, 44], the non-Fermi liquid (NFL) phase in 2CK Kondo model only survives in $0 < r_{max}$ region, where $r_{max} = 0.23$. The p-h asymmetry is irrelevant for $r > 0.23$. We will discuss pseudogap 2CK quantum phase transition by Kondo model and Anderson model as shown Fig.(1.15) and Fig.(1.16). The full (open) circles in diagrams are stable (unstable) fixed points and LM fixed means that local moment state. NFL represents non-Fermi liquid, ACR (SCR) represent critical p-h asymmetric (symmetric) point. For r=0 case, the lines of NFL fixed point represent non-Fermi liquid (over-screened Kondo effect, 2CK), it shows that flow is always towards NFL fixed point at any finite coupling. In the RG flows of 2CK pseudogap single impurity Kondo model as shown in Fig.(1.1.5): the horizontal axis denotes the renormalized Kondo coupling j, and renormalized potential scattering v which is representing particle hole asymmetry is the vertical axis. Dashed lines symbolize a flow out of the plane shown here.

For the metallic case (r=0), all lines flow into NFL fixed point at any finite coupling, 2CK governs the behaviors everywhere. LM is a unstable fixed point in the metallic case. In Fig.(1.15.b), the other non-Fermi liquid fixed point, NFL' represents a phase at large couplings and asymmetries. For $0 < r < r_{max}$, p-h asymmetry is irrelevant in non-Fermi liquid phase, a single p-h asymmetric NFL fixed point which separates NFL and NFL' fixed points is a asymmetric critical region (ACR). The LM fixed point is stable here, and a critical p-h asymmetric fixed point (SCR) controls the phase transition between LM and NFL fixed points. For $r > r_{max} = 0.23$ case, there is no NFL phase as shown in Fig.(1.15.b). The other LM phase, LM' fixed point represents a free local moment. The ACR fixed point controls phase transition between LM and LM' fixed points. The RG flows of the 2CK pseudogap single impurity Anderson model is shown in Fig.(1.16). The horizontal axis denotes the energy difference between spin and flavor impurity levels, the renormalized hybridization g is the vertical axis. The diagrams represent cuts, taken at $v = 0$, through the full RG flow. LM and LM' fixed points represent unscreened spin and free local moment phases, respectively. For r=0 case, the lines accessed to NFL fixed point at finite coupling ϵ, will access to LM fixed point (unstable) as $\epsilon \to \pm\infty$. For $0 < r < r_{max}$, LM (LM') fixed point becomes a stable fixed point. The NFL fixed point in Fig.(1.16.a) is replaced by ACR fixed point here, and two isolated p-h symmetric fixed point are located outside the $u = 0$ plane. The two SCR fixed points control phase transition between ACR and LM (LM') fixed point. For $r_{max} < r < 1$, the phase transition between LM and LM' can be controlled by ACR fixed point. The flow is towards to ACR fixed point as at $\epsilon = 0$. For $r \geq 1$, the transition is a level crossing, in other words, there is no QPT. Free impurity fixed point(FIMP) is located at $g = \epsilon = 0$, and flow is towards to FIMP at $\epsilon = 0$.

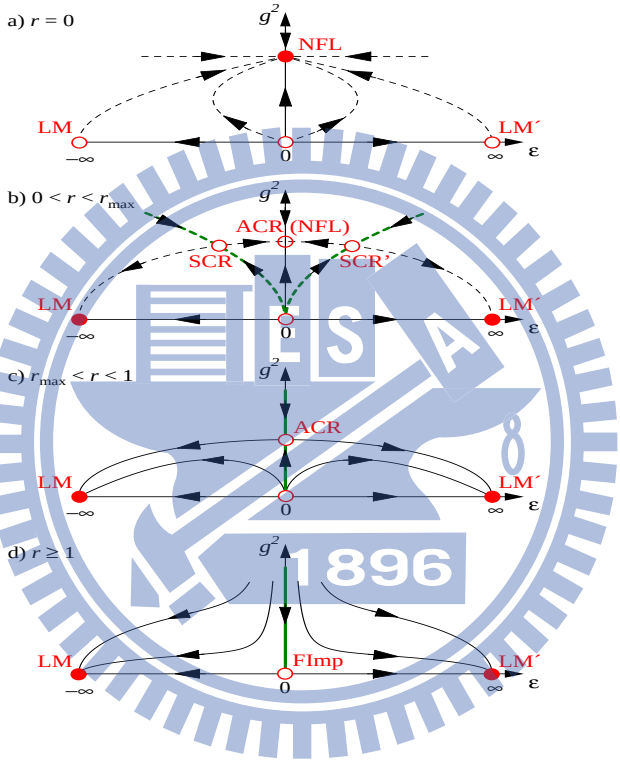

Figure 1.16: The RG flow phase diagram of 2CK particle-hole asymmetric single impurity pseudogap Kondo model. The details are in text. Adapted from [44].

Chapter 2

Large N Approaches To 2CK Anderson Model

The ground state and thermodynamic behaviors of s-d model represented by the the non-degenerate Anderson model can be understood by the Fermi liquid theory [5], conformal field theory [32, 54], the Bethe ansatz solutions [55], renormalization group, and numerical renormalization group [51, 56]. The QPT of pseudogap Kondo problems with the N-fold degenerate Anderson model analyzed by RG and NRG have been introduced in Chapter 1 [41, 43, 44]. Here, we introduce one of large N approaches, so called non-crossing approximation (NCA) to solve the N-fold degenerate Anderson model, where $N \to \infty$ is number of different spin flavor of fermions [57, 58, 60, 61]. The N-fold degenerate Anderson model with infinite U Coulomb potential can be solved by salve-boson representation [62]. The NCA approach has been successfully applied to Anderson impurity modes to address quantum field theory and critical phenomena. In this chapter, we will solve two-channel pseudogap Anderson model with infinite U Coulomb potential via NCA and salve-boson representation.

2.1 Methods To N-fold Degenerate Anderson Model

2.1.1 The Foundation Of Slave Boson Representation

For simplicity, we start from the Hamiltonian for N-fold degenerate infinite U Anderson model out of equilibrium [5],

$$H = E_0|0,0><0,0| + \sum_{\sigma} E_{1,\sigma}|1,\sigma><1,\sigma| + 1/2U \sum_{\sigma,\sigma',\sigma\neq\sigma'} n_\sigma n_{\sigma'} + \sum_{k,\sigma} \epsilon_k c^\dagger_{k,\sigma} c_{k,\sigma} \quad (2.1)$$
$$+ \sum_{k,\sigma} (V_k|1,\sigma><0,0|c_{k,\sigma} + V_k^* C_{k,\sigma}|0,0><1,\sigma),$$

where infinite U Coulomb potential leads to no doubly-occupied state. The index m (m=0,1) denotes the spin operator, spin up (m=0) or down (m=1). The diagrammatic perturbation theory does not work here, because $U \sim \infty$ goes beyond the validity of perturbation theory. The function for coupling strength function of dot and leads is

$$\Gamma^\sigma(\omega) = 2\pi \sum_{k,\sigma} |V_{k\sigma}|^2 \delta(\omega - \epsilon_{k\sigma}), \quad (2.2)$$

where $\Gamma^\sigma(\omega) = \Gamma\rho_c$, $\Gamma = \pi V^2_{k\sigma}$, and ρ_c is the conduction electron density of states. Now we express this model by Hubbard operators,

$$|1,\sigma><0,0| = \chi_{\sigma,0}, \quad |0,0><1,\sigma| = \chi_{o,\sigma}, \quad (2.3)$$
$$|0,0><0,0| = \chi_{0,0}, \quad |1,\sigma><1,\sigma| = \chi_{\sigma,\sigma}.$$

Diagrammatic approaches based on Wick's theorem can not be applied here, because the commutation relations, $[\chi_{p,q}, \chi_{q',p'}] = \chi_{p,p'}\delta_{q,q'} \pm \chi_{q,q'}\delta_{p',p}$. Nevertheless, the slave-boson representation [62] can solve these problem, where the χ operators are replaced by boson and fermion operators.

$$\chi_{\sigma,o} = f^\dagger_b f, \quad \chi_{0,\sigma} = f_\sigma b^\dagger, \quad (2.4)$$
$$\chi_{0,0} = b^\dagger b, \quad \chi_{\sigma,\sigma} = f^\dagger_\sigma f_\sigma,$$

where f and b operators are called pseudo-fermion and slave-boson satisfying the communication relation $[b, b^\dagger]_- = 1$ and anti-communication relation $[f_\sigma, f^\dagger_\sigma]_+ = \delta_{\sigma,\sigma'}$,

respectively. This approach enforce a local constraint to ensure no double occupy on the impurity,

$$Q = b^\dagger b + \sum_\sigma f_\sigma^\dagger f_\sigma = 1. \tag{2.5}$$

From this representation, the N-fold degenerate Anderson model becomes

$$H = \sum_\sigma \epsilon_f f_\sigma^\dagger f_\sigma + \sum_{k,\sigma}(V_k f_\sigma^\dagger c_{k,\sigma} b + V_k^* c_{k,\sigma}^\dagger f_\sigma b^\dagger) + \sum_{k,\sigma} \epsilon_k c_{k,\sigma}^\dagger c_{k,\sigma}. \tag{2.6}$$

The first two term are quadratic terms, and hybridization V_k can be a expansion parameter in perturbation theory. We provide more details on slave-boson representation and apply to study the 2CK infinite U Anderson model out of equilibrium in Section 2.2.

2.1.2 Non crossing approximation (NCA) approach

Non crossing approximation (NCA) approach is one of large N approaches to solve many-body system. Instead of having two flavors (N=2, spin=$\uparrow$ or $\downarrow$). This method assumes $N \to \infty$ flavors of fermions in conduction bath and on the impurity. In the limit of $N \to \infty$, one can self-consistently solve for Green functions of conduction electrons, impurity fermion and slave-boson, by including all self-energy diagrams with no lines crossing each other, so called NCA approach. Solutions via NCA are exact when $N \to \infty$. At a finite N ($< \infty$), we can systematically calculate the O(1/N) calculations to the large N solutions [58]. In the physical system where N=2 (not $N \to \infty$), large-N approach has been successfully used to provide qualitatively correct Kondo physics in a single-impurity Kondo problem. However, NCA always leads to NFL singular impurity DOS $\rho_\sigma(w)$ in any Kondo models. It does not correctly describe Fermi-liquid behavior of single channel Kondo system. A more accurate numerical approach, NRG can resolve this artifact. Nevertheless, NCA approach is able to correctly describe NFL behavior in multi-channel Kondo problems. In fact, NCA approach has been successfully applied to 2CK equilibrium and out of equilibrium system [57, 58]. The 2CK infinite U single impurity Anderson model out of equilibrium will be solved by NCA in Section 2.2.

2.2 The 2CK Pseudogap Anderson Model out of equilibrium

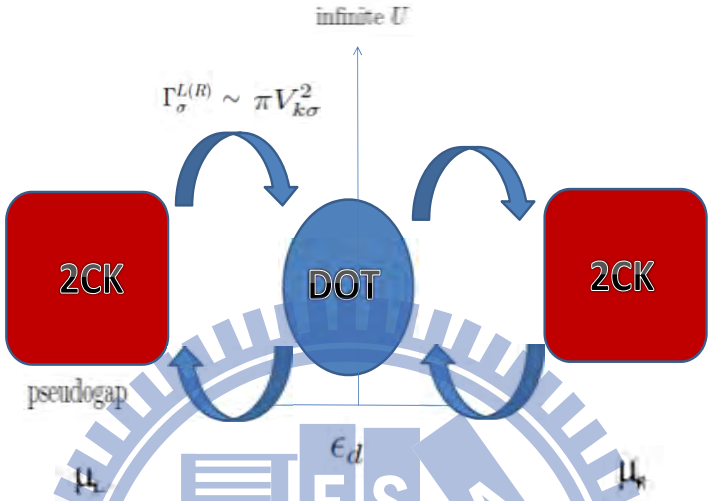

Figure 2.1: The set sup of 2CK pseudogap Anderson model out of equilibrium with strong Coulomb potential. There are two 2CK leads which couple to single QD out of equilibrium, where 2CK leads with pseudogap conduction electron DOS are in thermal equilibrium, respectively.

This section, we will solve non-equilibrium 2CK infinite U pseudogap single impurity Anderson model with $SU(M=2) \times SU(N=2)$ symmetry, where N and M is the spin degeneracy of impurity and number of electron reservoirs (or Kondo screening channels), respectively. Here, non-equilibrium system arises different coupling strength function of leads and dot different form Eq.(2.2). The pseudogap conduction electron density of states $\rho_c \sim |w|^r$ in the 2CK Anderson model corresponds constant density of states Anderson model for exponent r=0 [44, 61]. The schematic 2CK pseudogap Anderson model out of equilibrium was shown in Fig.(2.1). For simplicity, we start from the non-equilibrium

2CK single impurity Anderson model with constant DOS [57, 58],

$$H = \sum_{\tau,\alpha,\sigma,k} (\epsilon_{k\sigma} - \mu_\alpha) c^{\alpha\dagger}_{k\sigma\tau} c^{\alpha}_{k\sigma\tau} + \sum_{\sigma} \epsilon_\sigma d^\dagger_\sigma d_\sigma + \frac{1}{2} U \sum_{\sigma} \sum_{\sigma' \neq \sigma} n_\sigma n_{\sigma'} + \sum_{\tau,\alpha,\sigma,k} (V^{\alpha}_{k\sigma} c^{\alpha\dagger}_{k\sigma\tau} d_\sigma + H.C.) \tag{2.7}$$

There are different chemical potentials μ_α of left (α=L) and right(α=R) lead in non-equilibrium system, where $\alpha \in L, R$. Spin flavors are represented by $\sigma = 1, ...N$ and $\tau = 1, ...M$ corresponds to independent electron reservoirs. Here, we set $N = M = 2$. The $c^{\alpha\dagger}_{k\sigma\tau}$ ($c^{\alpha\dagger}_{k\sigma\tau}$) in Eq.(2.7) is the operator which creates (destroys) an electron in conduction electron Fermi sea with momentum k of left or right 2CK leads. The second term in Eq.(2.7) describes the spin σ electrons on the quantum dot, and the last two terms represent the electron Coulomb interaction on the quantum dot and leads-dot hopping, respectively. The retarded conduction electron Green function was defined as

$$G^r_c(t) = -i\theta(t) < \{c^\dagger_{k\sigma}(t), c_{k\sigma}(0)\} > . \tag{2.8}$$

The conduction electron density of states is the imaginary part of the retarded conduction electron Green function,

$$\rho_c(w) = ImG^r_c(t). \tag{2.9}$$

The coupling strength function (without pseudogap DOS) of dot and leads is $\Gamma^{L(R)}_\sigma(\omega) \sim \rho_c(w)$, it can be written as

$$\Gamma^{L(R)}_\sigma(\omega) = 2\pi \sum_{k \in L(R)} |V^\alpha_{k\sigma}|^2 \delta(\omega - \epsilon_{k\sigma} - \mu_\alpha). \tag{2.10}$$

The the chemical potential of two-channel non-equilibrium Anderson model is

$$\mu_\alpha = \mu_0 + (-)\frac{eV_\alpha}{2}, \quad \alpha = L(+), \quad \alpha = R(-), \tag{2.11}$$

where μ_0 is chemical potential of conduction baths, μ_α represents chemical potential with bias voltage (eV_α) of left or right lead. The Fermi function with bias voltage of left side or right side is

$$f_\alpha(w) = f(w + \mu_\alpha), \quad \alpha = L(+), \quad \alpha = R(-). \tag{2.12}$$

In non-equilibrium system, different chemical potentials (μ_L, μ_R) lead to different Fermi functions $(f_L(w), f_R(w))$. However, $\mu_L = \mu_R$ and $f_L(w) = f_R(w)$ correspond to equilibrium (zero bias). We consider Coulomb repulsion U to be infinite, giving no double

occupancy on the dot. In this case, our model does not show p-h symmetry, because of Coulomb repulsion is set to be $U \to \infty$ and $\epsilon_d \neq -1/2U$. The third term in Eq.(2.7) is a unperturbed term, where U is the infinite Coulomb interaction of electrons on the dot. Diagrammatic perturbation theory can not be used here as $U \to \infty$. The hybridization coupling $V^{\alpha}_{k\sigma}$ in Eq.(2.7) seems to be a more useful expansion parameter for perturbation theory. From Section 2.1, the infinite U Anderson model can be made quadratic by a transformation with the slave-boson and pseudo-fermion operators. Here, we define the slave-boson and pseudo-fermion operators, where $b^{\dagger}$ creates a empty state and $f^{\dagger}_{\sigma}$ ($\sigma =\uparrow or \downarrow$) creates a singly occupied state. The $d^{\dagger}_{\sigma}$ and d_{σ} in Eq.(2.7) can be decomposed as,

$$d_{\sigma}(t) = b^{\dagger}_{\tau}(t) f_{\sigma}, \tag{2.13}$$
$$d^{\dagger}_{\sigma}(t) = f^{\dagger}_{\sigma} b_{\tau}(t),$$

where σ is spin (up or down), and $c^{\dagger}_{\sigma} f^{\dagger}_{\sigma} |\Omega> = f^{\dagger}_{\sigma} b_{\tau} f^{\dagger}_{\sigma} |\Omega> = 0$, $|\Omega>$ is the vacuum state. Due to no double occupancy on the dot, we add a local constraint,

$$Q = b^{\dagger}_{\tau} b_{\tau} + \sum f^{\dagger}_{\sigma} f_{\sigma} = 1 \tag{2.14}$$

where Q is the total physical states, it must be equal to unity (Q=1). Now we rewrite the Hamiltonian in the slave-boson representation,

$$H = \sum_{k\sigma\tau\alpha} (\epsilon_k - \mu_{\alpha}) c^{\alpha\dagger}_{k\sigma\tau} c^{\alpha}_{k\sigma\tau} + \epsilon_d \sum_{\sigma} f^{\dagger}_{\sigma} f_{\sigma} + \sum_{k\sigma\tau\alpha} (V^{\alpha}_{k\sigma} (f^{\dagger}_{\sigma} b_{\tau} c^{\alpha}_{k\sigma\tau}) + H.C) \tag{2.15}$$

The first two terms in Eq.(2.13) are the unperturbed quadratic terms, and the last term is the hybridization. Diagrammatic perturbation theory can be used as hybridization $V^{\alpha}_{k\sigma}$ is a small expansion parameter. The Green function of pseudo-particles up to lowest order self-energy is shown in Fig.(2.2), where pseudo-fermion self-energy involves slave-boson propagator, and slave-boson self-energy involves pseudo-fermion propagator. Note that the Hamiltonian represented by salve-boson, pseudo-fermion and the local constraint are equivalent to Eq.(2.7). Since we study the non-equilibrium infinite U Anderson model, how to deal with the local constraint is an important problem here. We apply Keldysh diagrammatic perturbation theory to formulate our equations (see Ref. [57].) We start

from the action S_c in Q=1 ensemble, defined as:

$$S_c(-\infty,-\infty) = e^{-i\oint_c dt' H(t')} \tag{2.16}$$

Next, we write down the non-equilibrium partition function as,

$$Z_{Q=n} = Tr\{e^{-\beta(H_0-\mu_L N_L-\mu_R N_R)} \times \delta_{Q.n} T_c[S_c(-\infty,-\infty)]\}. \tag{2.17}$$

Here n=1, and T_C is the operator which orders operators along the Keldysh contour. If we have an operator $\hat{O}$, the expectation value in $Q=1$ ensemble is given by

$$< \hat{O} >_{Q=1} = \frac{1}{Z_{Q=1}} Tr\{e^{-\beta(H_0-\mu_L N_L-\mu_R N_R)} \times \delta_{Q.1} T_c[S_c(-\infty,-\infty)\hat{O}]\}. \tag{2.18}$$

We can rewrite $\delta_{Q,1}$ as an integral over a complex chemical potential $i\lambda$ [63]

$$\delta_{Q,1} = \frac{\beta}{2\pi}\int_{-\pi/\beta}^{\pi/\beta} d\lambda e^{-i\beta\lambda(Q-1)}. \tag{2.19}$$

Now we divide both numerator and denominator of $< \hat{O} >_{Q=1}$ by partition function $Z_{Q=0}$, it leads to

$$< \hat{O} >_{Q=1} = \frac{Z_{Q=0}}{Z_{Q=1}} < \hat{O} >_{i\lambda}^{(1)}. \tag{2.20}$$

There are two contributions in non-equilibrium expectation value of $\hat{O}$ in Q=1 ensemble, $< \hat{O} >_{i\lambda}^{(1)}$ and $\frac{Z_{Q=0}}{Z_{Q=1}}$, where

$$< \hat{O} >_{i\lambda} = \frac{1}{Z_{Q=1}} Tr\{e^{-\beta(H_0-\mu_L N_L-\mu_R N_R+i\lambda Q)} \times T_c[S_c(-\infty,-\infty)]\}, \tag{2.21}$$
$$< \hat{O} >_{i\lambda}^{(1)} = \frac{\beta}{2\pi}\int_{-\pi/\beta}^{\pi/\beta} e^{i\beta\lambda} < \hat{O} >_{i\lambda},$$

and

$$Z_{Q=0} = Tr\{e^{-\beta(H_0-\mu_L N_L-\mu_R N_R)} \times \delta_{Q.0} T_c[S_c(-\infty,-\infty)]\}, \tag{2.22}$$
$$\delta_{Q,0} = \frac{\beta}{2\pi}\int_{-\pi/\beta}^{\pi/\beta} d\lambda e^{-i\beta\lambda(Q)}.$$

As the trace of $< \hat{O} >_{i\lambda}$ divides by $Z_{Q=0}$, it does not restrict in Q=1 ensemble, and the normalization $Z_{Q=0\,Q=1}$ can be obtained from identity $< Q >_{Q=1} = 1$, where

$$\frac{Z_{Q=1}}{Z_{Q=0}} = < b^\dagger b >_{i\lambda}^{(1)} + \sum_\sigma < f_\sigma^\dagger f_\sigma >_{i\lambda}^{(1)}. \tag{2.23}$$

From these, the constraint Eq.(2.12) can be solved, and expectation value $< \hat{o} >^{1}_{i\lambda}$ can be obtained diagrammatically. And the impurity retarded Green function is

$$G^r_\sigma(r) = -i\theta(t) < \{d_\sigma(t), d^\dagger_\sigma(0)\} > . \tag{2.24}$$

It can be written as $G^r(t) = \theta(t)[G^>(t) - G^<(t)]$,

$$G^{r<}_\sigma(r) = i < \{d_\sigma(o), d^\dagger_\sigma(t)\} >, \tag{2.25}$$

$$G^{r>}_\sigma(r) = -i < \{d_\sigma(t), d^\dagger_\sigma(0)\} >, \tag{2.26}$$

where $G^<(t)$ is the impurity lesser Green function, and $G^>(t)$ is the impurity greater Green function.

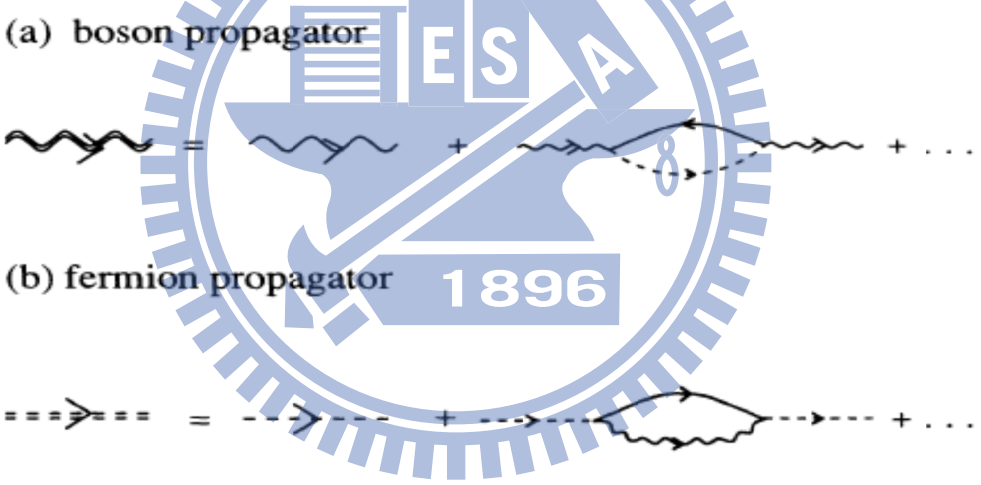

Figure 2.2: At lowest order, boson self-energy involves the fermion propagator, and fermion self-energy involves boson propagator. Adapted from [57].

The impurity spectral function is

$$\rho_\sigma(w) = -\frac{1}{\pi} Im G^r_\sigma(w), \tag{2.27}$$

where $G^r_\sigma(w)$ is the Fourier transform of the impurity retarded Green function. Due to infinite U potential, we need retarded Green function in the Q=1 ensemble with complex

chemical potential $i\lambda$,

$$\rho_\sigma(w) = -\frac{Z_{Q=0}}{Z_{Q=1}}|\frac{1}{\pi}ImG^{r(1)}_{\sigma,i\lambda}(w)| \tag{2.28}$$

Furthermore, we can write down the current though the dot,

$$J = \frac{e}{\hbar}\int d\omega \frac{2\Gamma_L(w)\Gamma_R(w)}{\Gamma_L(w)+\Gamma_R(w)}\rho_\sigma(w,V)\times[f(w+eV_\alpha/2 - f(w-eV_\alpha/2))] \tag{2.29}$$

Our goal is solve the current, therefore we have to analyze the impurity retarded Green function first, then density of states can be solved easily. Here, we expand $SU(2)\times SU(2)$ Anderson impurity model to $SU(N)\times SU(M)$ Anderson impurity model, where $N>2$ and $M>2$. We apply the large N approach, non-crossing approximation to our model on the Keldysh contour. The impurity retarded Green function in the Q=1 ensemble with $i\lambda$ can be expressed in terms of pseudo-particles within NCA approach, where neglects vertex relation.

$$\begin{aligned} G^{r(1)}_{\sigma,i\lambda}(t) &= -i\theta(t) < \{c_\sigma(t), c^\dagger_\sigma(0)\} >^{(1)}_{i\lambda} \\ &=^{NCA} -i\theta(t)[D^>(-t)G^<_{f\sigma}(t) - D^<(-t)G^>_{f\sigma}(t)]. \end{aligned} \tag{2.30}$$

Here, we define Green functions of pseudo-fermion:

$$\begin{aligned} G^>_{f\sigma} &\equiv -i < f_\sigma(t) f^\dagger_\sigma(0) >^0_{i\lambda}, \\ G^<_{f\sigma} &\equiv i < f^\dagger_\sigma(0) f_\sigma(t) >^1_{i\lambda}, \end{aligned} \tag{2.31}$$

and slave-boson:

$$\begin{aligned} D^> &\equiv -i < b_\tau(t) b^\dagger_\tau(0) >^0_{i\lambda}, \\ D^< &\equiv i < b^\dagger_\tau(0) b_\tau(t) >^1_{i\lambda}, \end{aligned} \tag{2.32}$$

where the natation $<$ and $>$ represents lesser and greater Green function. The fermion and boson propagators within NCA as shown in Fig.(2.3) are self-consistent via Dyson' equations , where the self-energies are iterated to all orders [57]. The lesser (greater) Green functions can be written as [59]:

$$\begin{aligned} D^{>(<)}(w) &= D^r(w)\Pi^{>(<)}(w)D^a(w), \\ G^{>(<)}_{f\sigma} &= G^r_{f\sigma}(w)\Sigma^{<(>)}_{f\sigma}(w)G^a_{f\sigma}, \end{aligned} \tag{2.33}$$

where $D^a(w)$ and $G^a_{f\sigma}$ is advanced Green function of boson and fermion, respectively. The advanced Green functions are complex conjugates of the retarded Green functions. The $\Pi^{>(<)}(w)$ is the self-energy of boson greater (lesser) Green function, and $\Sigma^{<(>)}_{f\sigma}(w)$ is the self-energy of fermion greater (lesser) Green function. The boson self-energies of lesser and greater Green function are given by (see Ref. [57, 60])

$$\Pi^{<}_b(w) = (-2i)\int_{-\infty}^{+\infty} d\epsilon G^{<}_{f\sigma}(\epsilon_d+\omega)[|V^L_{k\sigma}|^2]f(-\epsilon_d+\mu_L)\times \\ \rho_L(\epsilon_d-\mu_L-\mu_0)+[|V^R_{k\sigma}|^2]f(-\epsilon_d+\mu_R)\rho_R(\epsilon_d-\mu_R-\mu_0), \tag{2.34}$$

$$\Pi^{>}_b(w) = 2i\int_{-\infty}^{+\infty} d\epsilon G^{>}_{f\sigma}(\epsilon_d+\omega)[|V^L_{k\sigma}|^2]f(\epsilon_d-\mu_L)\times \\ \rho_L(\epsilon_d-\mu_L-\mu_0)+[|V^R_{k\sigma}|^2]f(\epsilon_d-\mu_R)\rho_R(\epsilon_d-\mu_R-\mu_0), \tag{2.35}$$

and fermion self-energies,

$$\Pi^{<}_f(w) = 2i\int_{-\infty}^{+\infty} d\epsilon D^{<}_{f\sigma}(\epsilon_d+\omega)[|V^L_{k\sigma}|^2]f(-\epsilon_d+\mu_L)\times \\ \rho_L(-\epsilon_d+\mu_L+\mu_0)+[|V^R_{k\sigma}|^2]f(-\epsilon_d+\mu_R)\rho_R(-\epsilon_d+\mu_R+\mu_0), \tag{2.36}$$

$$\Pi^{>}_f(w) = 2i\int_{-\infty}^{+\infty} d\epsilon D^{>}_{f\sigma}(\epsilon_d+\omega)[|V^L_{k\sigma}|^2]f(\epsilon_d-\mu_L)\times \\ \rho_L(-\epsilon_d+\mu_L+\mu_0)+[|V^R_{k\sigma}|^2]f(\epsilon_d-\mu_R)\rho_R(-\epsilon_d+\mu_R+\mu_0), \tag{2.37}$$

The relation between greater Green function and retarded Green function are, $D^{>}(w) = 2iImD^r(w)$, $G^{>}_{f\sigma} = 2iImG^r_{f\sigma}$, where the self-energies, $\Pi^{>}(w) = 2iIm\Pi^r(w)$ and $\Sigma^{>}_{f\sigma}(w) = 2iIm\Sigma^r_{f\sigma}(w)$. The retarded self-energies can be solved by greater self-energies, where

$$\Pi^r(w) = \frac{i}{2\pi}\int_{-\infty}^{+\infty} dw' \frac{\Pi^{>}(w)}{w-w'-i\eta} \tag{2.38}$$

$$\Sigma^r(w) = \frac{i}{2\pi}\int_{-\infty}^{+\infty} dw' \frac{\Sigma^{r}(w)}{w-w'-i\eta} \tag{2.39}$$

The retarded Greens function for pseudo-fermion is given by

$$G^r(w) = [w-\epsilon_d-\Sigma^r(w)]^{-1}, \tag{2.40}$$

and for slave-boson,

$$D^r(w) = [w-\Pi^r(w)]^{-}1. \tag{2.41}$$

The self-energy for pseudo-fermion,

$$\Sigma^r(w) = \frac{M}{\pi}\sum_\alpha \int d\epsilon \Gamma_\alpha(w-\epsilon-\mu_\alpha) f(w-\epsilon-\mu_\alpha) D^r(\epsilon), \tag{2.42}$$

and self-energy for slave-boson,

$$\Pi^r(w) = \frac{N}{\pi}\sum_\alpha \int d\epsilon \Gamma_\alpha(w-\epsilon-\mu_\alpha) f(w-\epsilon-\mu_\alpha) G^r(\epsilon). \tag{2.43}$$

The NCA expressions for the lesser Green of the pseudo-fermion is $G^<(w) = \sum^<(w)|G^r(w)|^2$ and slave-boson is $D^<(w) = \pi^<(w)|D^r(w)|^2$. The lesser Green function self-energy of pseudo-fermion is,

$$\Sigma^<(w) = \frac{M}{\pi}\sum_\alpha \int d\epsilon \Gamma_\alpha(w-\epsilon-\mu_\alpha) f(w-\epsilon-\mu_\alpha) D^<(\epsilon) \tag{2.44}$$

and of slave-boson,

$$\Pi^<(w) = \frac{N}{\pi}\sum_\alpha \int d\epsilon \Gamma_\alpha(w-\epsilon-\mu_\alpha) f(w-\epsilon-\mu_\alpha) G^<(\epsilon). \tag{2.45}$$

Within NCA approach onto Keldysh contour, we can solve self-consistent equations

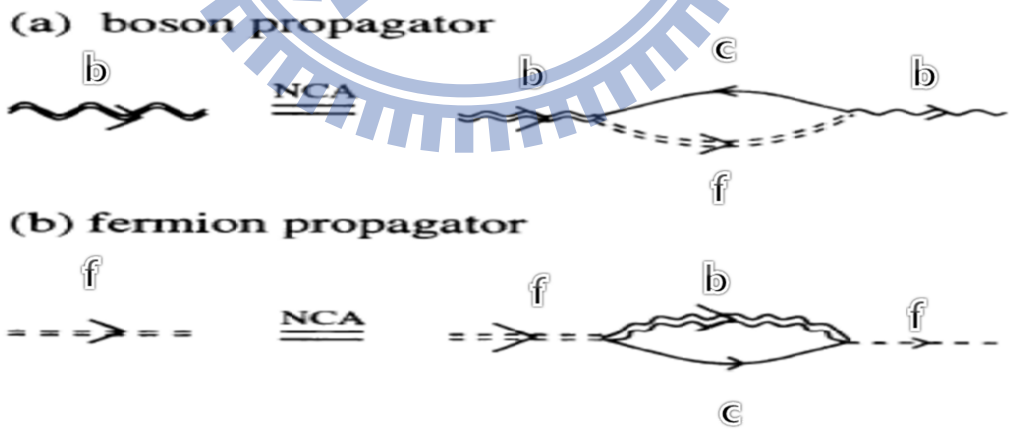

Figure 2.3: Diagrammatic self-consistent Dyson's equations, Eq.(2.38)-Eq.(2.41). Adapted from [58].

(Eq.(2.38)-Eq.(2.43)) numerically. Salving this self-consistent equations corresponds summing all order diagrams in matrix element V.

Now we couple pseudogap DOS to 2CK single impurity Anderson model as shown in Fig.(2.1). We assume pseudogap conduction-electron density of states is [60]

$$\rho_c(w) = -\frac{1}{\pi} ImG_c(w) = \frac{r+1}{2D^{r+1}}|\omega|^r \theta(D-|\omega|), \tag{2.46}$$

where vanish with power-law fashion. The G_c is conduction electron Green function, w in Eq.(2.44) is the momentum space of conduction electrons, D is half-band width, and r is the exponent of pseudogap. The 2nd term in 2CK constant DOS single impurity Anderson Hamiltonian (Eq.(2.7)) describes conduction electrons, which is coupled to Eq.(2.45) now. The coupling strength of leads and dot with pseudogap DOS is

$$\Gamma_\alpha(w) \equiv \Gamma_\alpha \rho_c(w) = [\pi {V^\alpha_{k\sigma}}^2 N(0)] \frac{r+1}{2D^{r+1}}|\omega|^r \theta(D-|\omega|), \alpha = L, R \tag{2.47}$$

The bare density of states, $\rho_c(w)$ is defined as $N^*(w) = N(w)/N(0)$ [58], and $\Gamma_{L(R)} = \pi |V^\alpha_{k\sigma}|^2 N(0)$, where $N(0)$ is bare density of states of per(pseudo) spin and channel, $U_L = U_R$, $\Gamma_L = \Gamma_R = \frac{\Gamma}{2}$. Here, N and M denote the number of spin and charge channels, and $f(w)$ is the Fermi function, where$f(w) = [1+e^{\beta w}]^-1$. The physical impurity spectral function, $\rho_\sigma(w, V)$, is the convolution of pseudo-fermion and slave-boson Greens function

$$\rho_\sigma(\omega, V) = \frac{i}{2\pi^2 Z} \int d\epsilon [ImD^r(\epsilon) G^<(\omega+\epsilon) - D^<(\epsilon) ImG^r(w+\epsilon)]. \tag{2.48}$$

The normalization factor $Z = \frac{i}{2\pi} \int d\omega [M \times D^<(\omega) - N \times G^<(\omega)]$ enforces the constraint, $< Q >= 1$. The current is given by

$$I(V) = N \frac{e}{\hbar} \int dw \frac{2\Gamma_L(w)\Gamma_R(w)}{\Gamma_L(w)+\Gamma_R(w)} \rho_\sigma(w, V) \times [f(w+eV/2) - f(w-eV/2)]. \tag{2.49}$$

The linear-response conductance is directly obtained from

$$G(0,T) = N \frac{e^2}{\hbar} \int dw \frac{2\Gamma_L(w)\Gamma_R(w)}{\Gamma_L(w)+\Gamma_R(w)} (-\frac{\partial f(w)}{\partial W}) \times \rho_\sigma(w, V=0). \tag{2.50}$$

And the nonlinear conductance G(V) is given by $\frac{dI(V)}{dV}$. From self-consistent equations, we can compute the convolution of impurity DOS by numerics. The results via self-consistent equations of graphene and constant density of states will be given in next section. The quantum critical phase transition of 2CK pseudogap Anderson model will discussed in chapter 3.

2.3 Constant Density of States And Doped Graphene

We have been introduced quantum phase transition of pseudogap Kondo problems via RG and NRG in Section 1.5. In this section, we show the numerical results of 2CK pseudogap Anderson model from NCA self-consistent equations (Eq.(2.40)-Eq.(2.45)). We briefly discuss the materials correspond to 2CK pseudogap leads [44, 41, 60, 61], it was separated into three cases:

1. r=0: metals, constant density of states,
2. r=1: magnetic doped graphene,
3. $0 < r < 1$: correspond possibly to semiconductor soft gap.

Among these three cases, we were attended in investigating quantum phase transition. From NCA solutions, we study QPT via impurity spectral function and differential conductance scaling. In next two subsections, we will show the results via NCA of graphene and constant DOS 2CK Anderson impurity model. The quantum criticality in the interval $0 < r < 1$ will be discussed in Chapter 3.

2.3.1 Results Of Constant Density Of States Anderson Model

The constant DOS Anderson model corresponds to the system where two independent electron reservoirs coupled to magnetic impurity, as introduced in Section.1.3.2. The DOS Anderson model have been introduced in Section 2.2, as Eq.(2.1) and Eq.(2.7) which is represented equilibrium and non-equilibrium case, respectively. Here, we show the results adapted from Ned S. Wingreen and Yigal Meir, PRB, 1993 [57]. The impurity DOS (Eq.(2.48)) can be solved numerically via the convolution of the lesser and greater Green function. As shown in Fig.(2.4), the impurity DOS for constant DOS Anderson model is illustrated in equilibrium and non-equilibrium system, respectively. There is non-Lorentzian Kondo peak at $w = 0$ in equilibrium system , which is shown as the solid cure. Note that: "Kondo peak of single channel Kondo screening is a Lorentzian peak, there is always non-Lorentzian Kondo peak in impurity DOS solved by NCA approach.

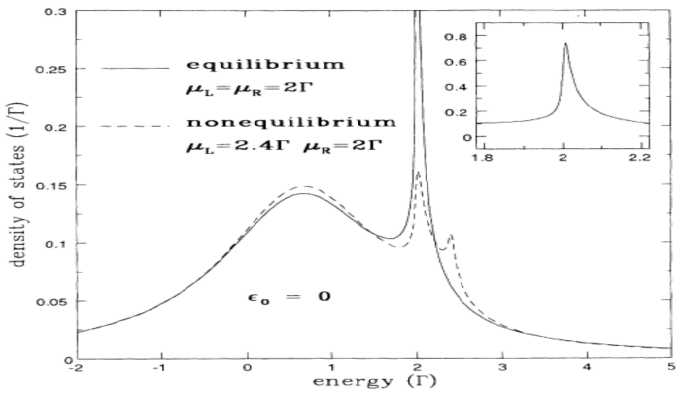

Figure 2.4: The impurity DOS $\rho_\sigma(w)$ for the r=1 2CK pseudogap Anderson model both in equilibrium and non-equilibrium system, where the magnetic impurity symmetrically coupled to leads of Lorentzian bandwidth 2W and chemical potential μ_R and μ_R. Note that: in our study, we use D to replace W to be half-bandwidth. Here, all energy is units of Γ, the coupling constant of leads and dot, the half-bandwidth at half-maximum is $W = 100$ and temperature $T = 0.005$. The dashed cure represents out of equilibrium impurity DOS, Kondo peak splits into two suppressed peaks. The p-h symmetric impurity DOS is shown as the solid line, where single Kondo peak is at $w = 0$. Adapted from Ref. [57].

The NCA approach is correct for 2CK". The dash line represents the impurity DOS out of equilibrium, where the Kondo peak is split up into two peaks by bias voltage. The width of two split peaks is equal to the quantity of bias voltage. The 2CK impurity DOS ave been successfully resolved by NCA approach, furthermore, we can solve the current and conductance by Eq.(2.49) and Eq.(2.40). The more details see Ref. [57, 58].

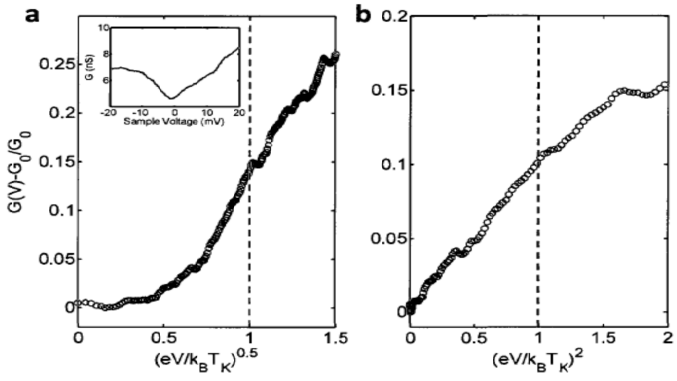

Figure 2.5: The scaling is characteristic of a Fermi liquid when $(eV/K_BT_k)^2$ plot. The conductance does not follow a linear behavior, when $(eV/k_BT_k)^{0.5}$ plot. Therefore, rule out spurious effects in the real 2CK behavior for type "π" Co impurities on graphene. Adapted from [6].

2.3.2 Results And Physics Of Doped Graphene

Graphene is honeycomb lattice structure with two inequivalent carbon atoms per unit cell. The two inequivalent carbon atoms were labeled by A and B sites. The momentum space of graphene is also honeycomb lattice structure. The band structure of graphene resolved by tight-binding method is called as Dirac core, because it satisfied Dirac equation and linear divergence. The point at $w = 0$ is called Dirac point. There are two independent Dirac cores of graphene in momentum space, their Dirac points labeled by K and K'. Experimentally, the adsorption Co atoms on heavily doped graphene lead to unusual Kondo resonances [6]. The experimental results of Ref. [6] show two-channel Kondo behavior as shown in Fig.(2.5). The QPT in doped graphene can be illustrated in a phase diagram as shown in Fig.(2.6), no Kondo screening in zero chemical potential [41]. Physical explanation for the effective low energy for magnetic impurities in graphene: " existence of two Dirac points are related to two independent Kondo screening channels". Note that: someone consider doped graphene is 1CK, because they believe two Dirac

core are scattering to each other at low temperature. The tight-binding description shows the hybridization between electron states in graphene and impurity states preserves the A-B sub-lattice symmetry [69]. The Co is located at the center of a graphene's hexagon [70], the inter valley scattering does not coupled to two screening channels, therefore effective 2CK ensues [68]". Theoretically, electrons in graphene provide a realization of two-dimensional Dirac electrons [41, 67]. Magnetic impurities coupled to two-dimensional Dirac electrons corresponds doped graphene [64, 65, 66], obeying the pseudogap conduction electron density of states ($\rho_c(w) \sim |w|^r$) , where exponent r=1. We use the 2CK infinite U Anderson impurity model (Eq.(2.1) and (Eq.(2.7)) to describes this model. It is worth mentioning: no vanishing gate voltage Kondo screening in graphene when weak coupling regime [41, 44, 45]. We can investigate doped graphene QPT by gate tuning as shown in Fig.(1.14.a).

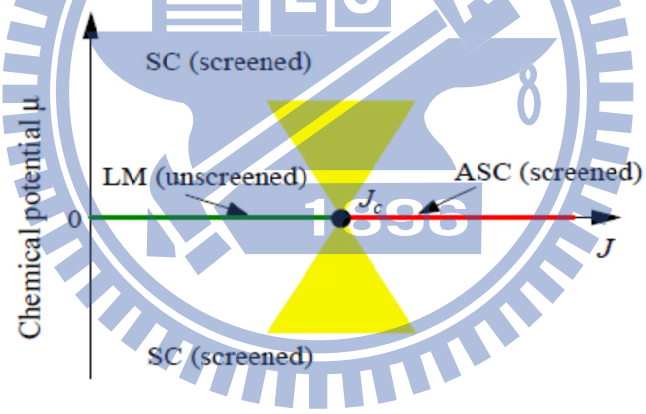

Figure 2.6: The quantum phase transition in graphene can be investigated by controlling the chemical potential μ_0. When $\mu = 0$, there is no 2CK state, always in LM state. If $\mu \neq 0$, the quantum phase transition between LM state and 2CK can be observed. Adapted from [41].

When chemical potential is zero ($\mu_0 = 0$), there is no Kondo screening. The QPT of graphene by gate controlled have been studied via NRG approach (see Ref. [41]). Here, we introduce QPT out of equilibrium of doped graphene with bias voltage by NCA

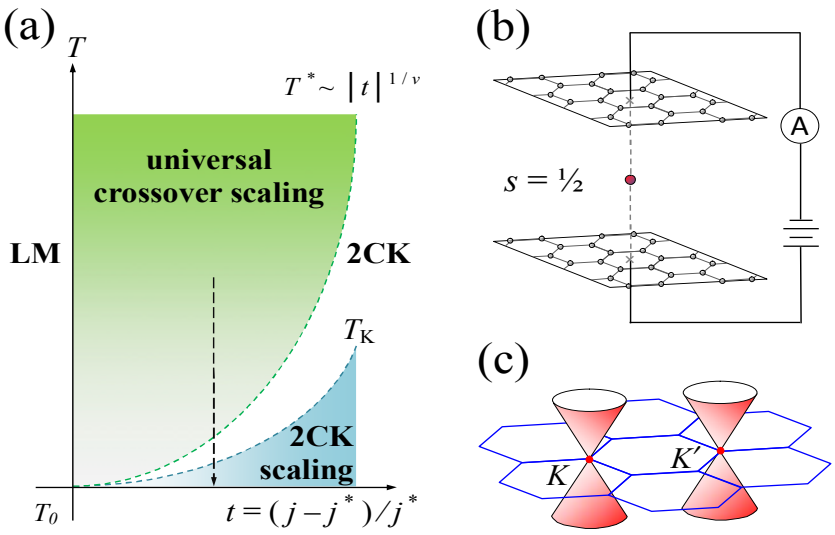

Figure 2.7: (a) The phase diagram for 2CK-LM crossover QPT, parameter j represents coupling Γ or chemical potential μ, and j^* is the crossover scale for a fixed temperature $T_0 = 5 \times 10^{-7} D$. All parameters in units of half-bandwidth D=1, and T_k and T_0 are energy scales associated with the 2CK universal scaling. (b) A spin one half impurity couples symmetrically to the two sub-lattices of two graphene leads out of equilibrium, where two graphene leads are in thermal equilibrium, respectively. (c) Doped graphene in momentum space. Adapted from [60].

solutions adapted from Section 2.2 [60]. The schematic setup. corresponds to Eq.(2.7) as shown in Fig.(2.7.b), a spin one half impurity (red dot) couples symmetrically to the two sub-lattices of two graphene leads, where different chemical potentials of each graphene. The two Dirac points at two independent Dirac Core corresponds to two Kondo screening channels as shown in Fig.(2.7.c). The diagram of QPT between LM and 2CK state as shown in Fig.(2.7.a) can be controlled by Γ and chemical potential, where Γ is the coupling constant of leads and dot ($|V_{k\sigma}^{\alpha 2}/\pi|$). The impurity spectral function which is the convolution of the greater and lesser Green functions is calculated via NCA equations numerically at different chemical potential as shown in Fig.(2.8). NCA solutions can provide correct physic results at Dirac point as two-channel Kondo. The impurity spectral function does not present p-h symmetry. The hight of Kondo peak is related to

Kondo temperature (T_k), and 2CK Kondo temperature is the function as [57]:

$$T_k \sim w(\Gamma/2\pi(\mu-\epsilon_d))^{1/2} exp[-\pi(\mu-\epsilon_d)/\Gamma]. \tag{2.51}$$

The parameters Γ and μ affect the the hight of Kondo peak. To analyze 2CK conductance scaling, we start form conductance behavior of two-channel Kondo. The most important property of 2CK conductance is the square root curve (see Section 1.2). Theoretically, we analyze two-channel Kondo conductance scaling function both of equilibrium and out of equilibrium [71]. First of all, we discus equilibrium system conductance, there is no bias voltage in system, and temperature dominates physics behavior, as a function G(0,T): a temperature dependent function formulated as,

$$G(0,T) - G(0,0) = B_c T^{\frac{1}{2}}, \tag{2.52}$$

where G(0,0) is a constant here, we have to omit this constant to observe square root curve in logarithmic scale. This analyzed function shows non-Fermi liquid behavior of two-channel Kondo in equilibrium. The non-equilibrium 2CK conductance scaling is formulated in terms of variable V and T,

$$G(V,T) - G(0,T) = B_c T^{\frac{1}{2}} H(A\frac{eV}{k_B T}). \tag{2.53}$$

The function $H(A\frac{eV}{k_BT})$ can be calculated by field theory, where $H(A\frac{eV}{k_BT}) \sim (\frac{eV}{k_BT})^2$ for $\frac{eV}{k_BT} << 1$, and $H(A\frac{eV}{k_BT}) \sim (\frac{eV}{k_BT})^{1/2}$ for $\frac{eV}{k_BT} >> 1$. In non-equilibrium case, temperature T is a constant as $T_0 = 5 \times 10^-7D$. From NCA equations, we numerically calculate doped graphene conductance both equilibrium and out of equilibrium. The results via NCA are shown in Fig.(2.9). Compare Fig.(2.9) to Fig.(2.5), there is comparison between theory and experiment. The Fig.(2.9.a) and Fig.(2.9.b) are the 2CK scaling of equilibrium conductance. The Fig.(2.9.c, d, e) are the 2CK scaling at different interval out of equilibrium.

Give a summaries of 2CK graphene universal scaling in conductance: In equilibrium, there is $\sqrt{T}$ behavior when $T < T_k$. In non-equilibrium system, there is $\sqrt{(eV/k_BT)}$ behavior when $T' < T < T_k$, and $(eV/k_BT)^2$ when $T' < T^*$, where T' is a small temperature. We have studied QPT of 2CK pseudogap Anderson model for r=0 and r=1 via

NCA. In next section, we will investigate quantum criticality and find universal scaling for $0 < r < 1$ bot

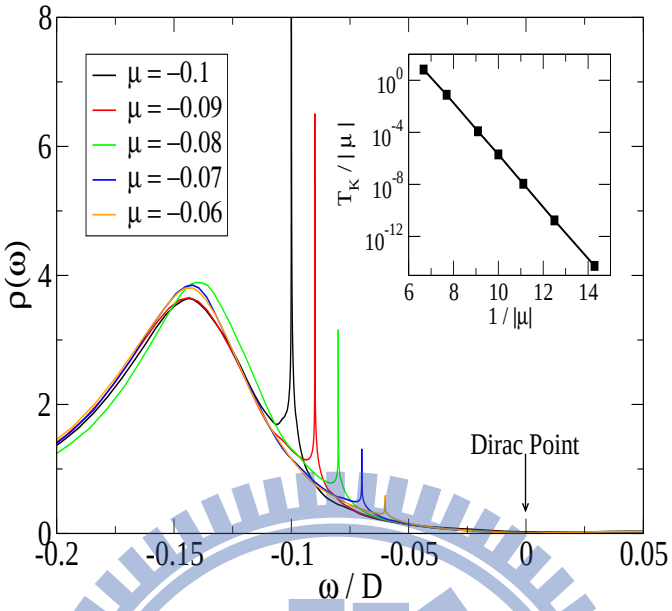

Figure 2.8: The impurity DOS via NCA v.s. different chemical potential μ in units of D. Dirac point is located at $w/D = 0$, and Kondo peaks are pinned near each μ. Different levels w/D with different chemical potentials μ correspond to different Fermi levels, respectively. The parameter are $T_0 = 5 \times 10^{-}7$D, $\Gamma = 0.2D$, $\epsilon_d = -0.2D$, where D is half-bandwidth. T_0 is temperature of the system, Γ is coupling constant of leads and dot, and ϵ_d is dot level. Adapted from [60].

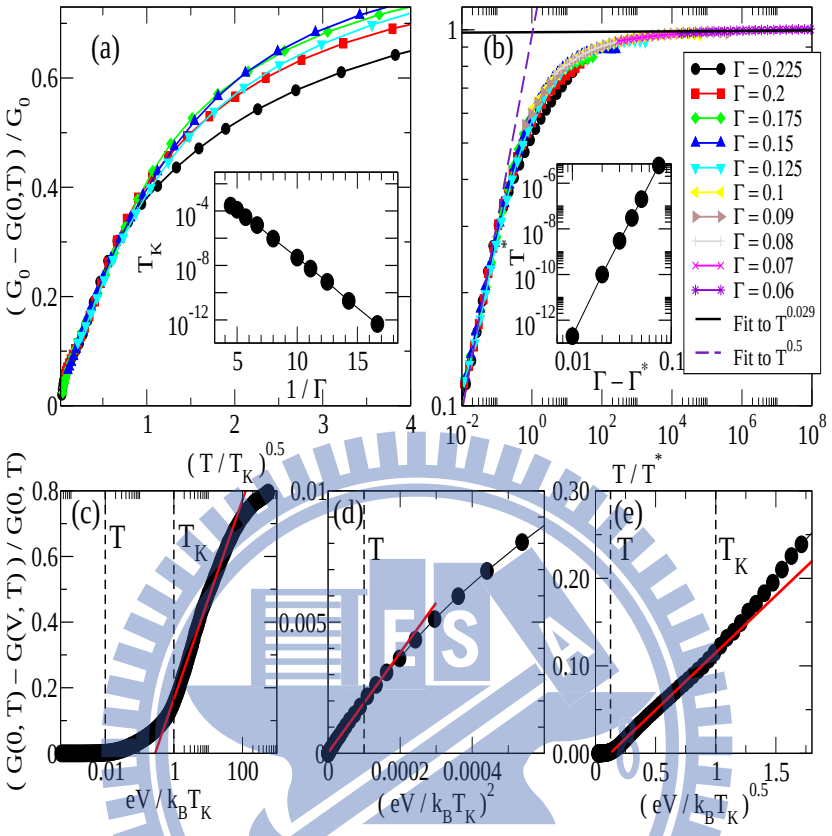

Figure 2.9: (a) The linear conductance in equilibrium system. It show square root behavior at temperature which is lower than Kondo temperature. (b) There is an additional power law behavior at high temperature in equilibrium conductance scaling. It shows $T^* \sim |\Gamma - \Gamma^*|^{1/\mu}$, where $\Gamma^*$is a small number, 0.05D and $\mu \sim 0.1$. (c) Nonlinear conductance at $\Gamma = 0.2D$. The fixed parameters are $T_0 = 5 \times 10^{-7}D, \mu = -0.1D, \epsilon_d = -0.2D$, where $D = 1$ is half-bandwidth. (d) The $(eV/k_BT)^2$ behavior arises as $(eV/k_BT) << T$. (e) The $(eV/k_BT)^{\frac{1}{2}}$ behavior arises as (eV/k_BT) is between T and T_K. Adapted from [60].

Chapter 3

Results Of The 2CK Pseudogap Anderson Model: Quantum Phase Transition and Quantum Criticality

In this chapter, we provide our NCA results for pseudogap 2CK Anderson model within quantum critical region for $0 < r < 1$. The 2CK QPT with pseudogap density of states have been investigated via renormalization group (RG) approach (see Section 1.3). Here, we investigate QPT in 2CK Anderson model by tuning exponent r via NCA approach. From impurity density of states (DOS), we analyze the quantum phase transition between LM and 2CK state and extract the quantum critical point. The differential conductance both in equilibrium and non-equilibrium cases are analyzed in Section 3.2. From our numerical results in conductance, we find the universal scaling at and near quantum criticality. The schematic phase diagrams of equilibrium and non-equilibrium are summarized in Fig.(3.1). The quantum critical point is at and near $r \to r_c \simeq 0.115$. The phase diagrams describe equilibrium and non-equilibrium crossover between LM and 2CK with crossover scales being T^* and V^*, respectively. Both equilibrium and out of equilibrium phase diagrams in conductance show power law divergence at quantum critical region. We also observe different universal scaling behavior between equilibrium and out

of equilibrium systems.

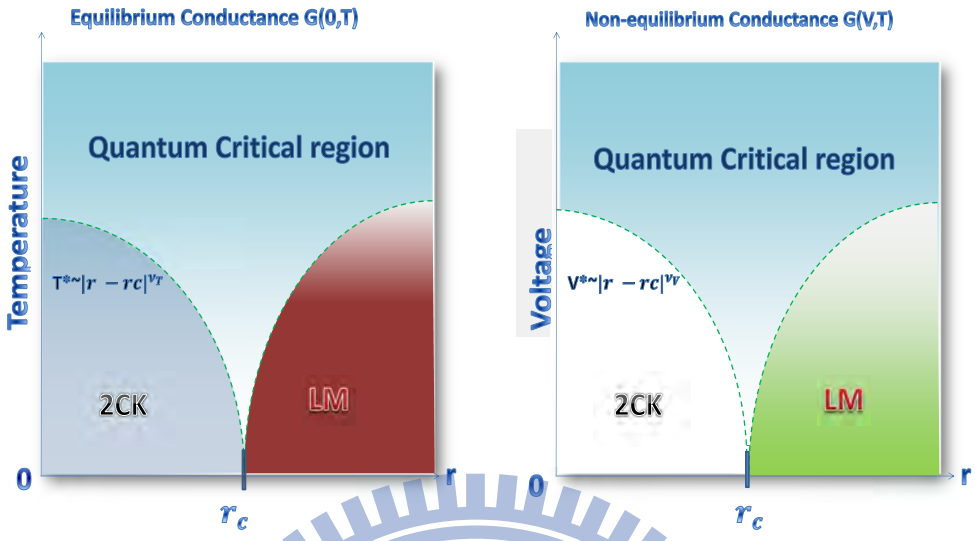

Figure 3.1: The phase diagram of equilibrium and non-equilibrium conductance. The phase diagrams delineated by T^* and V^*, which is crossover scale in equilibrium and out of equilibrium, respectively. The inverse of crossover scale is correlation length, ξ, which is diverge in quantum critical region, and $\nu_T = 4$, $\nu_V = 0.5$ are universal factor called as correlation length exponent. Due to ν_T, ν_V are different, the universal scaling in equilibrium is different from out if equilibrium. Here, critical point is at and near $r_c = 0.115$, even if G(0,T) and G(V,T) have slightly different parameters (Γ and ϵ_d).

3.1 Quantum Criticality Shows In Impurity Density Of States

The pseudogap DOS ($\rho_c(w)$) of conduction electrons vanishes in power law fashion at Fermi energy ($\rho_c \sim |\omega|^r$). If there is sufficient conduction electron DOS to screen the

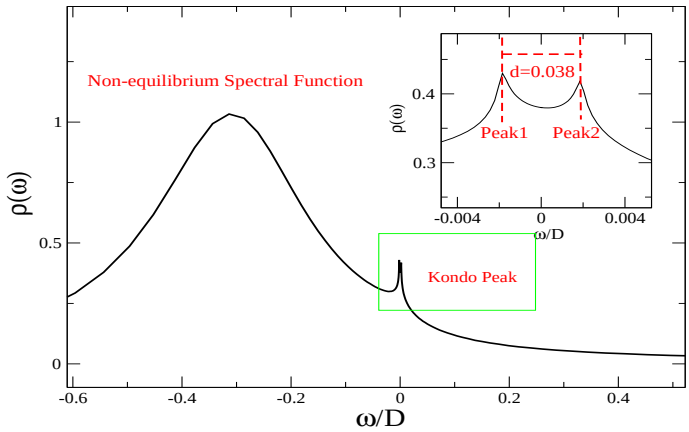

Figure 3.2: The r=0.05 density of states of impurity non-equilibrium system with $\Gamma = 0.3D, \epsilon_d = -0.3D, T = T_0 = 5 \times 10^{-7}D$, where $D = 1$. The impurity DOS exhibits asymmetry graph, where no peak at $_d + U$ due to particle-hole asymmetry. The non-equilibrium density of states with bias, $V = 0.038D$, Kondo peak divided into two peaks, because the Fermi energy of left and right leads are different, the width between two peaks is equal to bias.

magnetic impurity in 2CK system, the ground state is going to 2CK fixed point. On the other hand, it leads to LM fixed point if conduction electron DOS is not sufficiently large. Here, we study quantum phase transition of pseudogap 2CK Anderson model by tuning r $(0 < r < 1)$ at $\mu_0 = 0$ with fixed parameters Γ and ϵ_d, where μ_0 is chemical potential of the conduction bath. Not that: There is no Kondo screening in graphene (r=1) if $\mu_0 = 0$. We investigate quantum critical region form analyzing numerical data via NCA. In this chapter, we define two-channel Kondo temperature, T_{2CK}. In quantum dot system, three important features arise as 2CK ground state emerges $(T < T_{2CK})$,

1. The entropy of impurity spin $(S(\Omega))$ at $T \to 0$ is that $S(\Omega = 2) \simeq k_B ln\sqrt{2}$, where T is the temperature of the system,

2. A non-Lorentzian Kondo peak occurs at Fermi level in impurity DOS.

3. As $T < T_{2Ck}$, the conductance follows the scaling function Eq.(2.51) and Eq.(2.52).

From the 2nd feature of 2CK, we study impurity DOS for extract the critical point at and near r_c in this section. The conductance behavior and the universal scaling will be discussed in Section 3.2. The non-equilibrium impurity for r=0.05 is shown in Fig.(3.2), where Kondo peak is spilt up into two peaks due to bias voltage. We find Kondo peak in impurity DOS for r=0.05 is short, because QPT between 2CK and LM leads to Kondo peak shorter as r is close to r_c more and more. The impurity DOS for different r is demonstrated in Fig.(3.3.a), it exhibits QPT between LM and 2CK by varying r in Kondo peak (Fig.(3.3.b)). Numerically, we can not address zero temperature, so $T_0 = 5 \times 10^{-7} D$ is used to approach to zero temperature, where T_0 **is the lowest numerically accessible temperature**. The Kondo peaks are shorter as r increases ,and there is a dip of Kondo peak for $r > 0.13$, we predict that LM state occurs while $r > 0.13$. The height of Kono peak is related to Kondo temperature which is as a function in Eq.(2.51). We can predict the critical point form the change of Kondo peaks. In order to study the quantum phase transition of two-channel pseudogap Anderson model both in equilibrium and non-equilibrium cases, we choose two sets of parameters to do so.

1. Equilibrium: $\Gamma = 0.28D$, $\epsilon_d = -0.2D$, zero bias voltage, varying temperature T, and the lowest temperature $T = T_0$,

2. Non-equilibrium: $\Gamma = 0.3D$, $\epsilon_d = -0.3D$, $T_0 = 5 \times 10^{-7} D$, varying bias voltage V,

when we study QPT in non-equilibrium conductance with bias voltage, temperature of the system is fixed at T_0. The parameter Γ ($\sim V^2/\pi$) is the coupling strength of leads and dot, ϵ_d is the dot level, and D=1 is half bandwidth. The parameters Γ and ϵ_d all affect 2CK Kondo temperature. But we find critical point is at and near $r_c = 0.115$ both in parameter $\Gamma = 0.28D$, $\epsilon_d = -0.2D$ and $\Gamma = 0.3D$, $\epsilon_d = -0.3D$. thus forecast quantum critical point is fixed as Γ and ϵ_d does not change too much. From the change of Kondo peaks for different r in impurity DOS, the QPT is observed and we can extract quantum critical region and critical point. Furthermore, we find the universal scaling both of equilibrium and non-equilibrium conductance in the quantum critical region, these details will be discussed in next section.

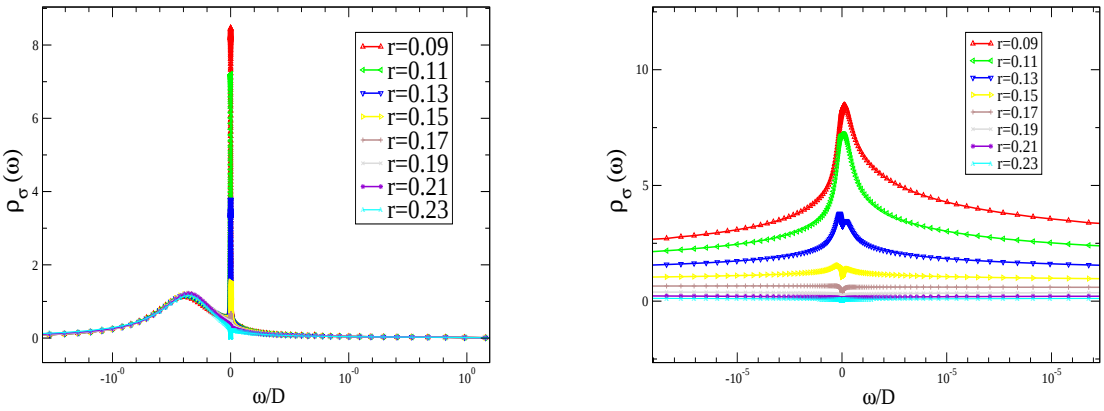

(a) Full DOS

(b) Kondo peaks

Figure 3.3: The Kondo peak of impurity spectral function with $\Gamma = 0.28D5, \epsilon_d = -0.2D$, and $T_0 = 5 \times 10^{-7}D$ by varying exponent r. (a) The full impurity DOS with p-h asymmetry. (b) Kondo peaks for different r in Fig.(3.3.a).

3.2 Conductance near LM-2CK Quantum Critical Point

In Section 3.1, the quantum phase transition is signaled by the diversification of Kondo peaks for different r in impurity DOS at $r \sim r_c$, as a result, we extract the critical point $r_c \simeq 0.15$. From the 3rd feature of 2CK in last section, we analyze conductance in special case of 2CK pseudogap Anderson model ($0 < r < 1$) to observe QPT between LM and 2CK. The behavior of 2CK conductance in the constant DOS Anderson model and graphene have been introduced in Section 1.3.2 and Section 2.3. In the next two subsections, we will discuss conductance and their universal scaling behavior, more details both in equilibrium and non-equilibrium cases for $0 < r < 1$. We further compare that the universal scaling in equilibrium and out of equilibrium. The conductance in equilibrium is a function of temperature T, G(V=0,T), most contribution comes from thermally excited electrons near Fermi surface. On the other hand, most contribution in non-equilibrium system comes from electrons excited by V. As a result, different Fermi energy in left and right right leads may lead to different G(V,T_0) as a function of V from that in equilibrium, G(0,T). In our study, we set $T = T_0 \sim 5 \times 10^{-7}D$ as the lowest numerically accessible temperature. We study further the universal scalings in conductance in quantum critical

region.

3.2.1 Equilibrium Conductance G(0.T)

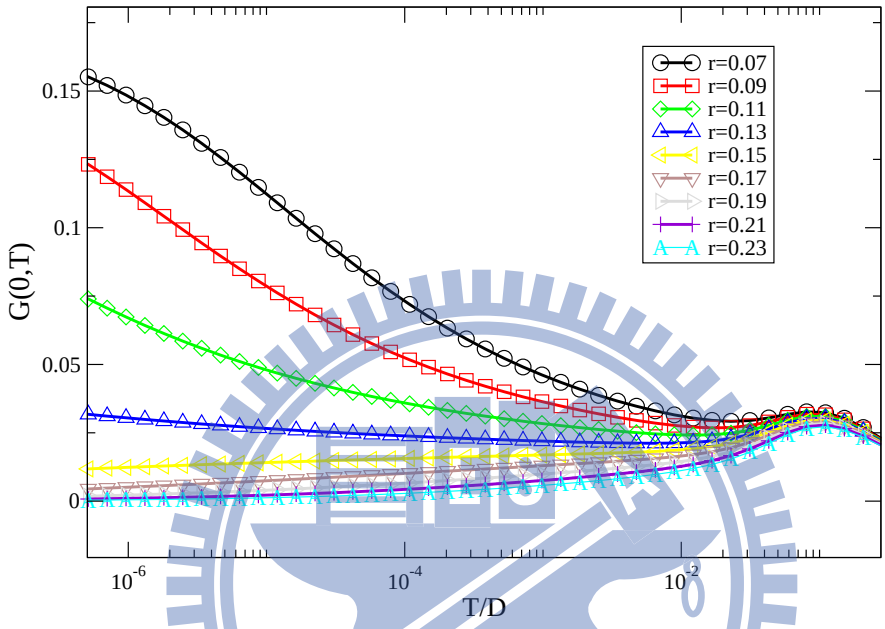

Figure 3.4: The conductance v.s. T with varying r in equilibrium system , where $\mu = 0$, $\Gamma = 0.28D$, $\epsilon_d = -0.2D$ are fixed, and the half-bandwidth D=1.

Here, we focus on conductance of 2CK pseudogap Anderson model for $0 < r < 1$ in equilibrium ($V = 0, T > 0$). As shown in Fig.(3.4), it exhibits G(0,T) by varying T for different r with $\Gamma = 0.28D$, $\mu_0 = 0$, $\epsilon_d = -.2D$, and $D = 1$. We expect that it follows the 2CK scaling function $G(0,T) - G(0,0) = B_c T^{\frac{1}{2}}$ in 2CK regime, therefore it exhibits $\sqrt{T}$ behavior at $T < T_k$. Numerically, we can not exactly address zero temperature system, therefore $G(0,0) \simeq G(0,\mathrm{T}_0 = 5\times10^{-7}\mathrm{D})$. The 2CK scaling behavior of differential conductance for different r exhibits $\sqrt{T}$ as shown in Fig.(3.5). However, the region of $\sqrt{T}$ scaling gets narrow as r increase. In Fig.(3.5), the $\sqrt{T}$ behavior is clear for r=0 , but almost disappears for $r \to 0.11$. We find the reason that G(0,T) deviates more and more from $\sqrt{T}$ behavior (violet dash line) as $r \to r_c$, because the system approaches to the G(0,T) is expected to show quantum critical point where a universal power law scaling

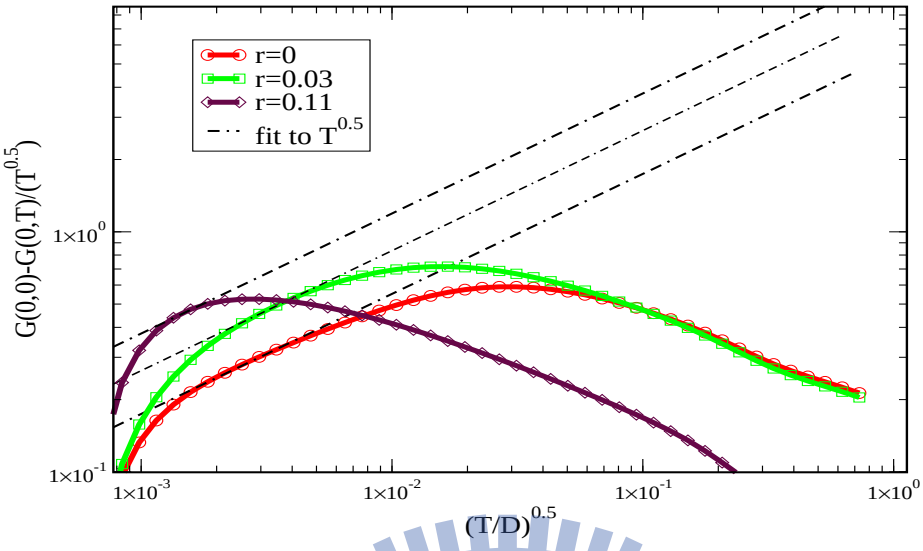

Figure 3.5: To illustrate $G(0,T) - G(0,0) = B_k T^{\frac{1}{2}}$ scaling for $0 < r < 1$, but we can't get a reasonable result. The $\sqrt{T}$ behavior of differential conductance is obvious for small r, but it gradually disappears as r increase. Here, T_d is the non-universal factor, and $\mu = 0$, $\Gamma = 0.28D$, $\epsilon_d = -0.2D$, $D = 1$.

in T. As shown in Fig.(3.6), we find the power of conductance for each exponent r in Fig.(3.5) are related to $|r - r_c|$ at the interval between $5 \times 10^{-4}D$ and $5 \times 10^{-7}D$. We define the power in conductance for each r between $5 \times 10^{-4}D$ and $5 \times 10^{-7}D$ as σ_T. There is a linear relationship between $|r - r_c|$ and σ_T, where $r_c = 0.115$. The region between $5 \times 10^{-4}D$ and $5 \times 10^{-7}D$ is expect to show the quantum criticality. So we suppose that the conductance $G(0,T) \equiv G_{QCP}(0,T)$ at quantum critical region, which is analyzed as:

$$G_{QCP}(0,T) \sim T^{\sigma_T} = T^{\beta_T - \alpha_T |r - r_c|}, \tag{3.1}$$

where β_T and α_T are non-universal factors, $T^{\sigma_T} = T^{\beta_T}$ as $r = r_c$. Next, $G(0,T)$ divides by T^{σ_T}, then it becomes

$$\widetilde{G}(0,T) = G(0,T)/T^{\sigma_T} = \frac{G(0,T)}{T^{\beta_T - \alpha_T |r - r_c|}}, \tag{3.2}$$
$$\widetilde{G}_{QCP}(0,T) = G_{QCP}(0,T)/T^{\sigma_T} = constant.$$

The curves between Eq.(3.1) become flat. We rescale y axis ($\widetilde{G}(0,T)$) by a non-universal

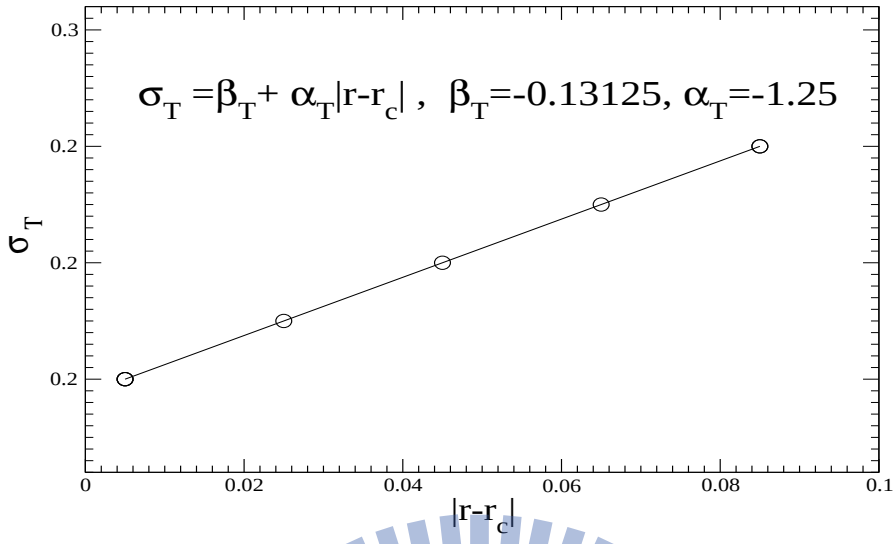

Figure 3.6: To illustrate σ_T v.s. $|r - r_c|$ plot with $\mu = 0$, $\Gamma = 0.28D$, $\epsilon_d = -0.2D$, where$D = 1$.

factor d_0 such that every flat in y-axis overlap in the same value. Furthermore, x-axis is rescaled by factor T^* for normalization, the universal scaling is

$$\overline{G}(0, \frac{T}{T^*}) \equiv \frac{G(0, \frac{T}{T^*})}{(T/T^*)^{\beta_T - \alpha_T |r - r_c|} d_0}, \tag{3.3}$$

where T^* is inverse of correlation length ξ,

$$T^* \propto \frac{1}{\xi} = |r - r_c|^{\nu_T}, \tag{3.4}$$

ν_T is the power exponent of T^*. The universal scaling as Eq.(3.3) is shown in Fig.(3.7). As $r \to r_c$, correlation length $\xi \to \infty$, the scaling is the universal function. And the crossover scale can be described by T^*. As $r \to r_c$, $T^* \simeq 0$, there is quantum criticality. The universal scaling in equilibrium for $0 < r < 1$ normalized by T^* was shown in Fig.(3.8). The T^* V.S. $r - r_c$ plot was shown in Fig.(3.8). Fig.(3.8) in the logarithm scale shows linear relationship between T^* and $|r - r_c|$. The results of conductance in equilibrium for $0 < r < 1$ can be described as a phase diagram as shown in Fig.(3.1.a). The quantum critical region diverges in power law fashion as r_c. In summary, the QPT in equilibrium with $\mu_0 = 0$ can be observed by tuning exponent r and T. There is $\sqrt{T}$ scaling at $T < T_K$, but it become more and more narrow as r increases. Conductance

at region between $5 \times 10^{-4}D$ and $5 \times 10^{-7}D$ is universal. The QPT in non-equilibrium system will be discussed in next subsection .

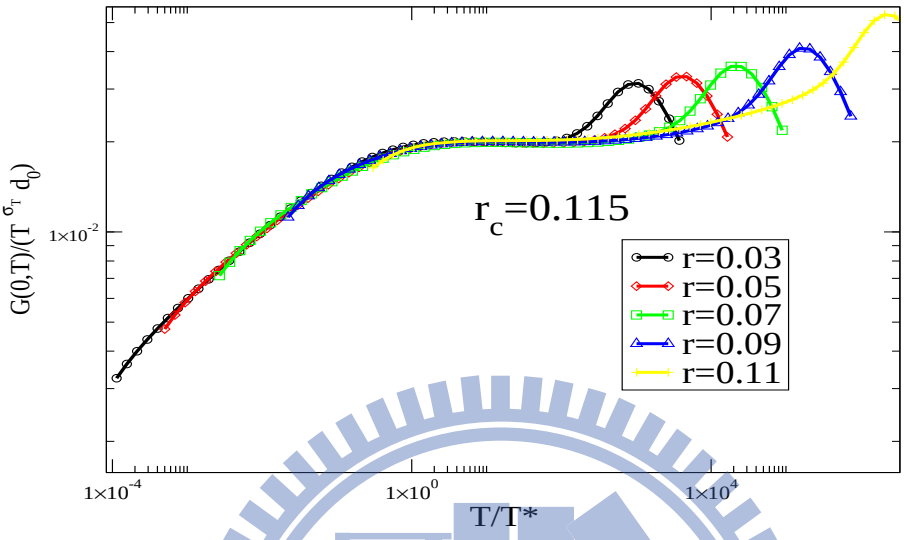

Figure 3.7: The universal scaling in G(0,T) is given by Eq.(3.1) with $\Gamma = 0.28D$, $\epsilon_d = -0.2D$ and $\mu = 0$, where$D = 1$. Set$r = 0.115$ is the critical point.

3.2.2 Non-equilibrium Conductance G(V,T_0)

In this section, we investigate quantum phase transition of the 2CK pseudogap Anderson model out of equilibrium for $0 < r < 1$ described by Eq.(2.15) via NCA approach. In particular, we address universal scaling in non-equilibrium conductance near quantum critical point. Here, we analyze conductance by adding bias voltage at fixed low temperature $T_0 \sim 5 \times 10^{-7}D$. For simplicity, we focus on the simple case with parity symmetry (left and right side), where $\Gamma_L = \Gamma_R = \frac{\Gamma}{2}$, and $\mu_L = \mu_R = eV/2$. The conductance G(V,T_0), is shown in Fig.(3.10), with $\Gamma = 0.3D$, $\epsilon_d = -0.3D$ at fixed temperature $T_0 \sim 5 \times 10^{-7D}$. As shown in Fig.(3.9), the conductance for each r saturates at low bias region, and we find that it follows 2CK scaling function for small r and $T < T_k$: $G(V,T) - G(0,T) = B_c T^{\frac{1}{2}} H(A\frac{eV}{k_B T})$, where the universal function $H(A\frac{eV}{k_b T})$ is $(\frac{eV}{k_B T})^2$ for $\frac{eV}{k_B T} << 1$ and $(\frac{eV}{k_B T})^{1/2}$ for $\frac{eV}{k_B T} >> 1$. In other words, in the 2CK regime, the conductance

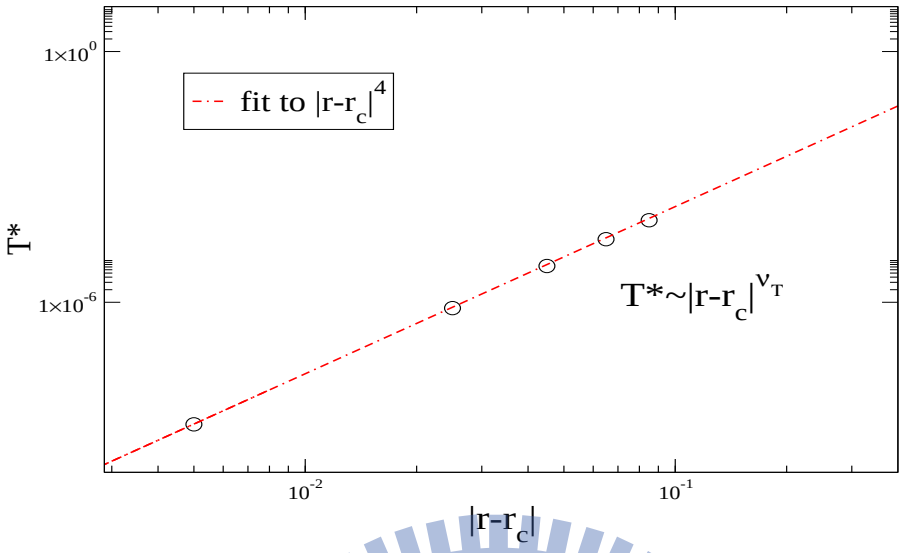

Figure 3.8: Crossover scale T^* v.s. $r - r_c$ plot with $\Gamma = 0.28D$, $\epsilon_d = -0.2D$ and $\mu = 0$, where$D = 1$.

should exhibits $\sqrt{eV/k_BT}$ and $(eV/k_BT)^2$ scaling behavior as $T < T_k$. The differential scaling in conductance is shown in Fig.(3.10), and it exhibit non-Fermi liquid behavior $\sqrt{V}$ at $\widetilde{T}_0 < V < T_k$, and V^2 for small bias region $V < \widetilde{T}_0$. The region gets narrow more and more as r increases. For r=0.03, it exhibits the obvious $\sqrt{eV/k_BT}$ and $(eV/k_BT)^2$ behavior, but the curve for r=0.07 shows clear deviations from $\sqrt{eV/k_BT}$ and $(eV/k_BT)^2$. The deviation is due to the fact that the system is close to the 2CK-LM quantum critical point, where distinct of universal scaling function is expected to show. In our study, the exponent r=0.115 is at and near critical point r_c. We analyzed the power σ_V in conductance for each r between V=$5 \times 10^{-3}D$ and $5 \times 10^{-5}D$. As shown in Fig.(3.11), there is linear relationship between σ_V and $|r - r_c|$ as $r \to r_c$, where a red dashed line is fitted to $|r - r_c|^1$. In quantum critical regime, the region between V=$5 \times 10^{-3}D$ and $5 \times 10^{-5}D$ which exhibits power law behavior in conductance is expected to show. So we suppose that $G(V, T_0) \equiv G_{QCP}(V, t_0)$ at the quantum critical region which can analyzed as:

$$G_{QCP}(V, T_0) \propto V^{\sigma_V} \sim V^{\beta_V + \alpha_V |r - r_c|}, \tag{3.5}$$

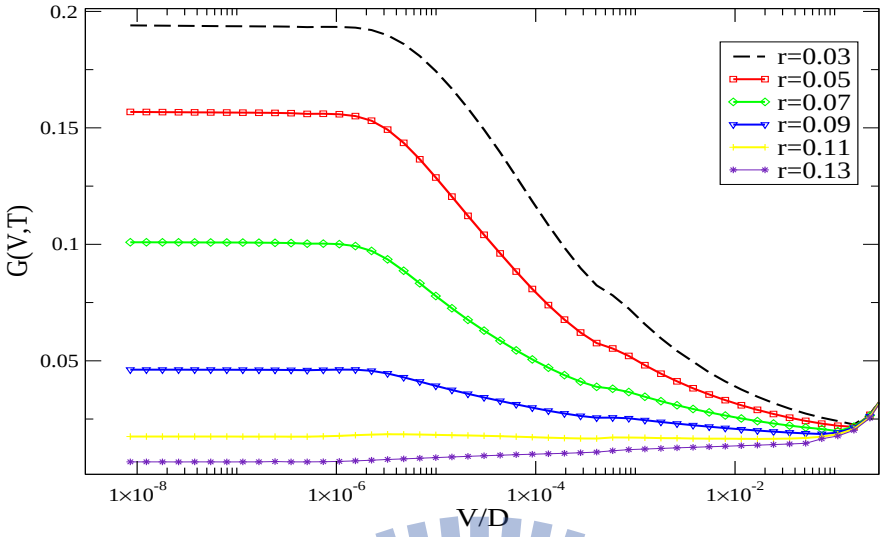

Figure 3.9: Non-equilibrium conductance of 2CK pseudogap Anderson model. G(V,T) saturates at a constant value for $V << T$, other parameters are $T = T_0 = 5 \times 10^{-7}D$, $\epsilon_d = -0.3D$ and $\Gamma = 0.3D$, $D = 1$. The bias voltage V is in unit of half-bandwidth D.

where β_V and α_V are non-universal factor. We find $\beta_V = 0$, $\alpha_V = -5$. AS $r \to r_c$, $\sigma_V \sim 0$. Next, The conductance G(V,T_0) divides by V^{σ_V}, then it becomes

$$\widetilde{G}(V,T_0) = G(V,0)/V^{\sigma_V}, \tag{3.6}$$
$$\widetilde{G}_{QCP}(V,T_0) = \frac{V^{\alpha_V|r-r_c|}}{V^{\sigma_V}} = constant.$$

Eq.(3.6) for different r becomes flat curves. Furthermore, we rescale y-axis $\widetilde{G}_{QCP}(V,T_0)$ by a non-universal factor d_0, therefore, each curve for different r overlap in the same value, where scaling in conductance is

$$\widehat{G}(V,T_0) \propto \frac{G(V,0)}{V^{\sigma_V} d_0} = \frac{V^{\alpha_V|r-r_c|}}{V^{\sigma_V} d_0}. \tag{3.7}$$

We rescale x-axis by V^* for normalization, the universal scaling is

$$\widehat{G}(\frac{V}{V^*},T_0) \propto \frac{G((\frac{V}{V^*},0)}{(V/V^*)^{\sigma_V} d_0} = \frac{(V/V^*)^{\alpha_V|r-r_c|}}{(V/V^*)^{\sigma_V} d_0}, \tag{3.8}$$

as shown in Fig.(3.12). Here, V^* is inverse of the correction length, ξ_V,

$$V^* \propto \frac{1}{\xi_V} = |r-r_c|^{\nu_V}. \tag{3.9}$$

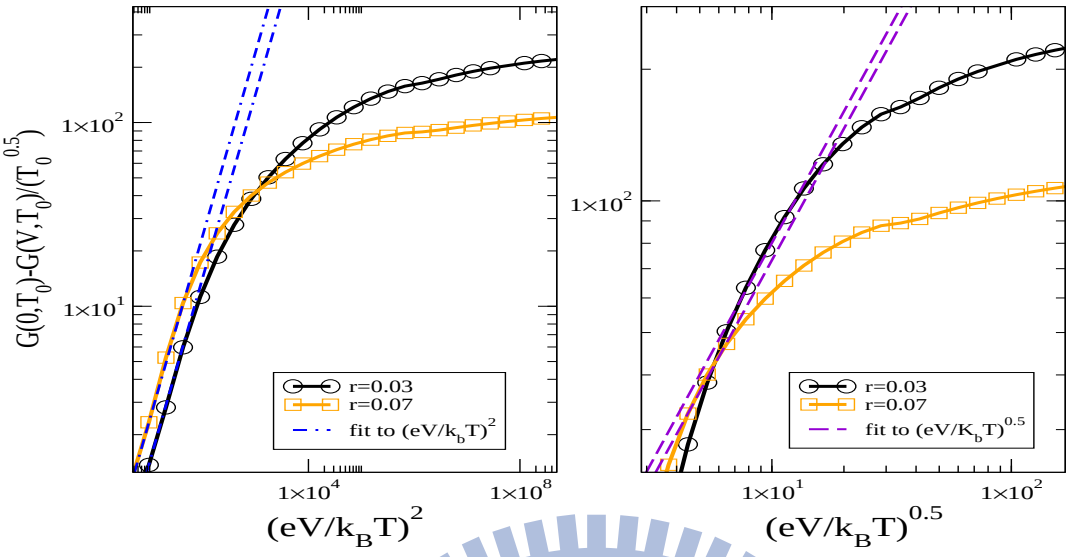

Figure 3.10: Scaling of non-equilibrium conductance, G(V,T) follows Eq.(2.53). The parameters are set as $T = T_0 = 5 \times 10^{-7}D$, $\epsilon_d = -0.3D$ and $\Gamma = 0.3D$, $D = 1$. The scaling exhibits the square root and square behavior of eV/k_BT, but reduced as exponent r increases.

To illustrate the quantum phase transition between LM and 2CK regimes, V^* describe the crossover state in power-law fashion. As $r \to r_c$, $V^* \sim 0$, there is quantum criticality, no crossover regime. The V^* v.s. $|r - r_c|$ plot is shown in Fig.(3.13), and it exhibits power-law behavior as r is close to r_c. This power is fitted to $|r - r_c|^{0.5}$, where $\nu_V = 2$. For r close to r_c, Eq.(3.9) is the universal function, and the result can be summarized by Fig.(3.1.b). In summary, the QPT in non-equilibrium for $0 < r < 1$ sets $\mu_0 = 0$ and which can be observed by tuning r and V. The differential conductance scaling exhibits $\sqrt{V}$ behavior at $T < T_K$ and V^2 behavior at $V < T$. But it deviates the differential conductance scaling function (Eq.(2.53)) as exponent r increases. The region between V=$5 \times 10^{-3}D$ and $5 \times 10^{-5}D$ is universal. We have studied the QPT for r=0, r=1, and $0 < r < 1$ both in equilibrium and non-equilibrium conductance. The QPT behavior of 2CK pseudogap Anderson model is manifest.

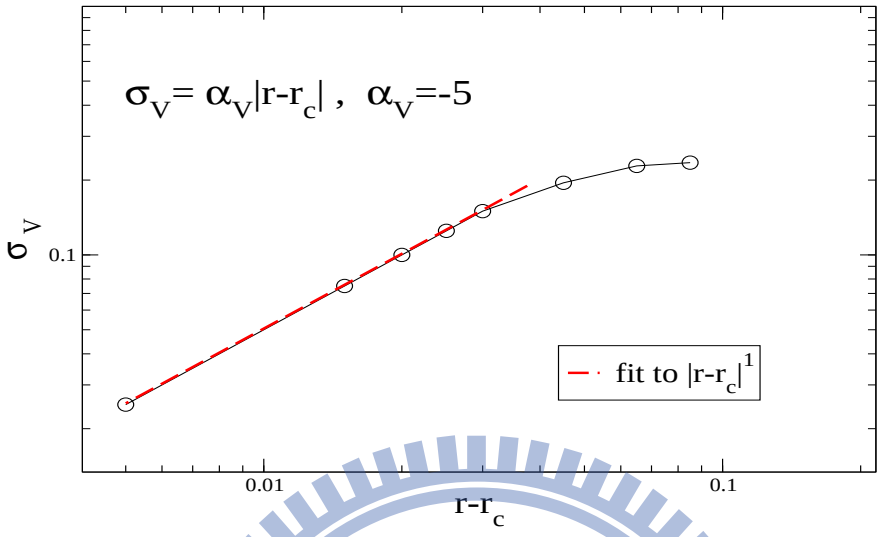

Figure 3.11: σ_V v.s. $|r - r_c|$ plot with $\mu = 0$, $\Gamma = 0.3D$ and $\epsilon_d = -0.3D$. We set D=1.

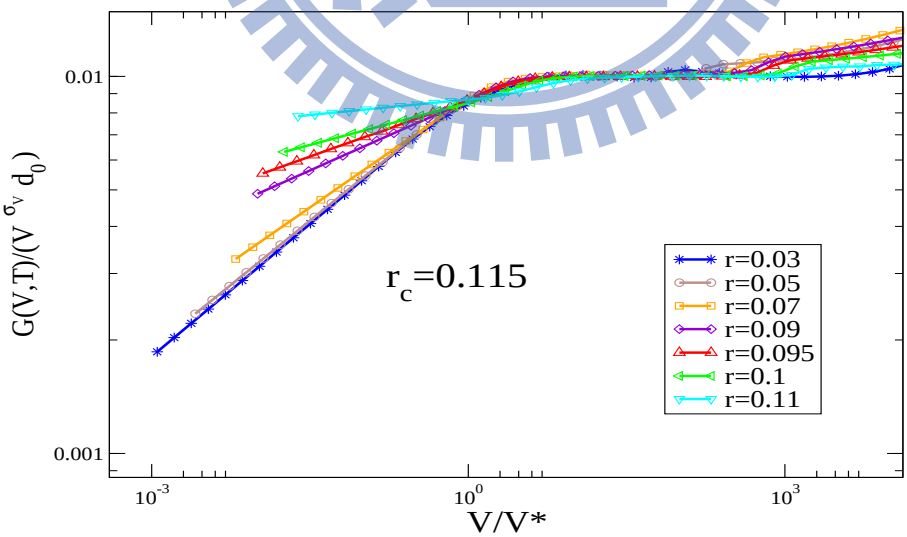

Figure 3.12: The non-equilibrium universal scaling in conductance for different r at low temperature, $T = 5 \times 10^{-7}D$. we set dot level $\epsilon_e = -0.3D$, $\Gamma = 0.3D$, and D=1.

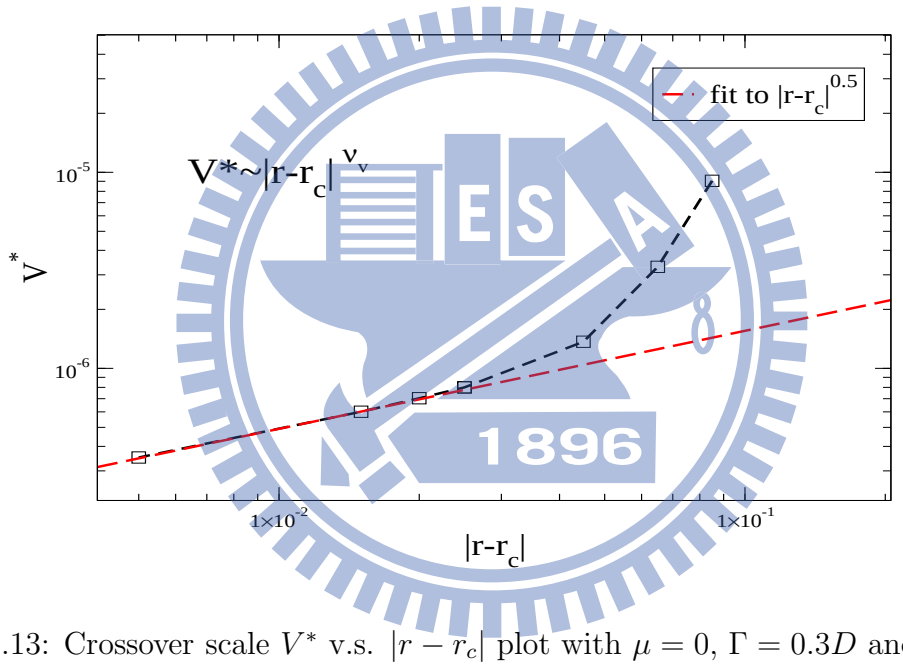

Figure 3.13: Crossover scale V^* v.s. $|r - r_c|$ plot with $\mu = 0$, $\Gamma = 0.3D$ and $\epsilon_d = -0.3D$. We set D=1.

Chapter 4

Summary And Conclusion

In recent years, there has been numerous studies of quantum phase transition (QPT) in condensed matter physics, especially the QPT between Kondo and other phases. With the improvement of nano-material fabrication, we are able to observe Kondo effect in quantum dot (QD) system. There are many examples of QPT of Kondo effect, such as: double quantum dot (DQD) system, two-channel Kondo effect (2CK) and pseudogap Kondo model. For DQD system, the competition between Kondo and RKKY coupling leads to the QPT between Kondo effect and spin singlet. For 2CK system, two independent electron sources exist and hence two-Kondo coupling constants J_1 and J_2 are needed to label the interactions, i.e. the Kondo screening from the two electron baths. There is a competition between J_1 and J_2, both of them simultaneously want to screen the impurity; therefore, leads to the QPT between two independent electron reservoirs. As a quantum dot couple to pseudogap conduction electron bath, the conduction electron density of states (DOS) $\rho_c \sim |w|^r$ vanishes at $w = 0$ in power-law fashion, where $0 \leq r \leq 1$. In our study, we investigate QPT by the 2CK pseudogap Anderson model with $0 < r < 1$ via large N slave-boson NCA approach both in equilibrium and non-equilibrium cases. In the 2CK pseudogap Anderson model, the constant DOS Anderson model corresponds to r=0, and r=1 for doping graphene. Note that: in our study, dope graphene is a 2CK system. The region $0 < r < 1$ possibly corresponds to semiconductor with soft gap. We employ slave-boson representation to solve infinite-U Anderson model, and self-consistently solve

for Green functions of impurity and slave-bosons, by including all self-energy diagrams with no lines crossing each other, so-called NCA. Numerically, we investigate the QPT by the impurity DOS and conductance via NCA equations both in equilibrium and non-equilibrium cases. The impurity DOS $\rho_\sigma(w)$ via NCA exhibits non-Lorentzian Kondo peak at $w = 0$. Kondo peak is separated into two peaks due to bias voltage, and the width between two peaks is equal to the amount of bias. The QPT between LM and 2CK can be observed by emergence of the dip of Kondo peaks for $r > r_c$. From the dip of Kondo peak in the impurity DOS at $T = 5 \times 10^{-7}D$, $V = 0$, we define the critical point which is at and near $r_c \simeq 0.115$. The 2CK feature in QD is defined in the differential conductance scaling as shown in Eq.(2.52) and Eq.(2.53). Here, we rewrite the 2CK differential conductance scaling as,

$$\begin{aligned} &\frac{G(0,T) - G(V,T)}{T^\alpha} = \kappa Y(\frac{eV}{k_B T}), \\ &Y(x) = 1 - F_2CK(x/\pi) \approx \frac{\pi}{3}\sqrt{x} \quad for \quad x >> 1, \\ &Y(x) = 1 - F_2CK(x/\pi) \approx cx^2, \quad c \approx 0.0758 \quad for \quad x << 1, \end{aligned} \tag{4.1}$$

with $\kappa = (g_0/2)(\pi/T_{2CK})^\alpha$, and $\alpha = 0.5$ for 2CK. We discover that the region satisfied Eq.(4.1) becomes narrower for $0 < r < 1$ both in equilibrium and non-equilibrium situations. The conductance both in equilibrium and non-equilibrium are analyzed as shown in Eq.(3.1) and Eq.(3.6), respectively. The universal scaling in equilibrium conductance for $0 < r < 1$ satisfies Eq.(3.3), and Eq.(3.5) describing the universal crossover scale between LM and 2CK phase, as shown in Fig.(3.1.a). On the other hand, Fig.(3.1.a) is the phase diagram in non-equilibrium for $0 < r < 1$, the crossover scale is described by Eq.(3.10), and Eq.(3.9) is the universal scaling out of equilibrium. In our study, we find the hybridization does not influence the critical point too much for $0 < r < 1$ as shown in Fig.(3.1.a) and Fig.(3.1.b). The QPT for $0 < r < 1$ can be described by distance to criticality in terms of both $|r - r_c|$, T (equilibrium) and V (non-equilibrium). We choose two sets of parameter in equilibrium and non-equilibrium, but we find the same critical point $r_c = 0.115$.

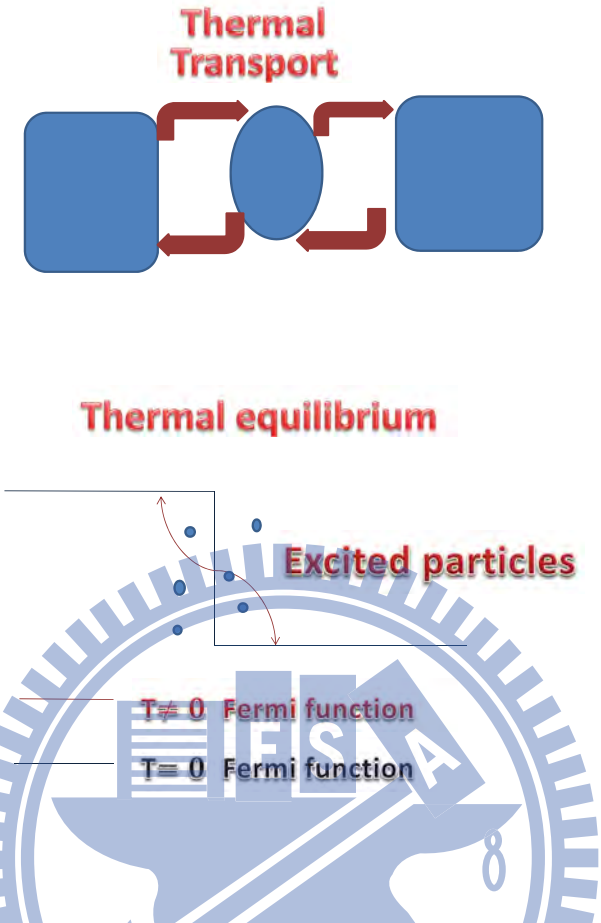

Figure 4.1: This figure depicts the equilibrium thermal transport and Fermi function. Red line represents $T \neq 0$ Fermi function, where particles may be excited by thermal energy.

For the cases for r=0 and r=1, there have been many studies and the QPT between LM and 2CK by tuning Γ and μ_0 are well-known. We investigate the QPT between 2CK and LM for $0 < r < 1$ and find the universal scaling both in equilibrium and non-equilibrium cases. And we find out that the scalings of G(V,$T_0 \sim 0$) and G($V = 0$,T) are different, even if V and T are exchanged. We discover that the universal scaling in equilibrium and non-equilibrium are not identical. The conductance G(0,T) is a function of T, within results from thermally excited electrons near Fermi surface as shown in Fig.(4.1). As shown in Fig.(4.2), the conductance in non-equilibrium system is mostly coming from those electrons excited by the bias voltage V, leading to different Fermi energy in left and right leads. The difference between the conductance scaling in equilibrium G(V,$T_0 \sim 0$) and non-equilibrium G(V=0,T) can be understood by this argument. The QPT both in equi-

librium and out of equilibrium are summarized in a three dimensional phase diagram as shown in Fig.(4.3), it exhibits different universal scaling behavior in equilibrium and out of equilibrium, respectively. In experiments, we can investigate non-equilibrium system with the advancement of nano-technology in recently years. The non-equilibrium system becomes an important subject in condensed matter both in experiments and theory. Our study provides theoretical basis for further study in Kondo break down, quantum criticality and non-Fermi liquid behavior in condensed matter systems.

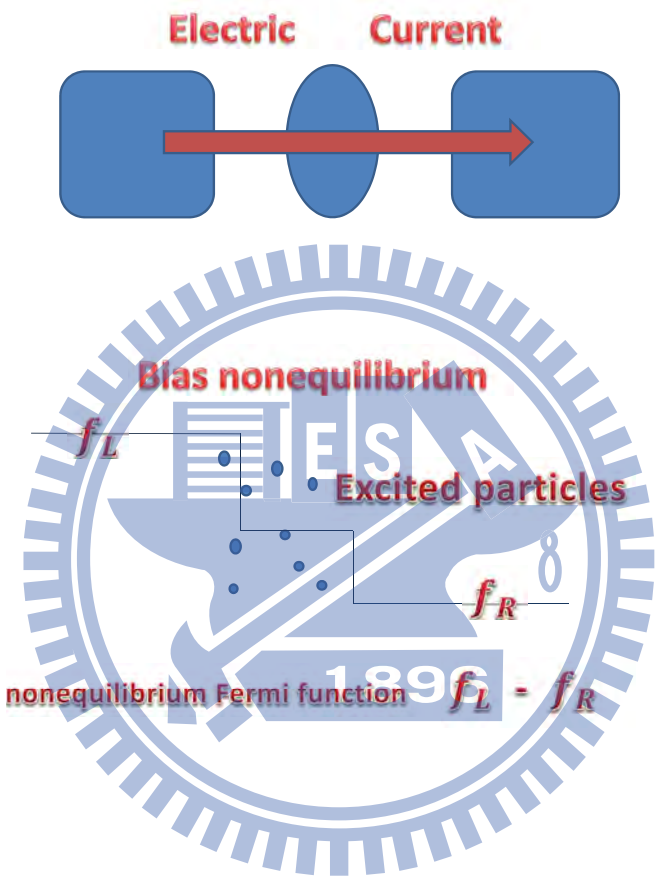

Figure 4.2: The non-equilibrium transport in our system depends on current. The Fermi function for non-equilibrium case is different from the one in equilibrium because of the difference between chemical potential of the left and right leads. Fermi function of the left and right are different. The Fermi function of non-equilibrium system shows a jump $f_L - f_R$ across the impurity.

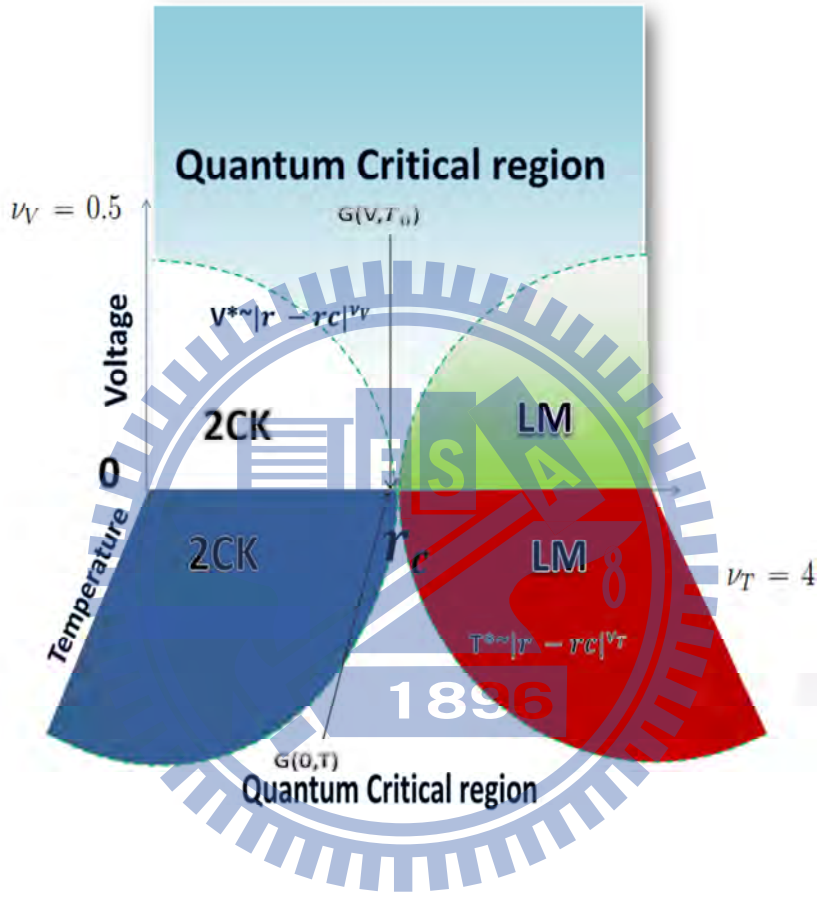

Figure 4.3: The three dimensional phase diagram to describe QPT between LM and 2CK both in equilibrium (G(0,T)) and out of equilibrium (G(V,T_0)). The quantum criticality can be accessed either by G(0,T) in equilibrium and or by G(V,T_0) out of equilibrium. The equilibrium and non-equilibrium conductance show distinct scalings at criticality.

Appendix A

Here, we give a supplemental material: discussion for two-channel Kondo effect. We think about a simple model out of equilibrium where two leads couple to a quantum dot, where

$$H = \sum_{k\sigma\alpha} \epsilon_{k\sigma}(C^{\alpha\dagger}_{k\sigma}C^{\alpha}_{k\sigma} - \mu_\alpha) + \sum_{\sigma} \epsilon_\sigma d^\dagger_\sigma d_\sigma + \frac{U}{2}\sum_{\sigma} \epsilon_d d^\dagger_\sigma d_\sigma + \sum_{k\sigma\alpha}(V^\alpha_{k\sigma}C^{\alpha\dagger}_{k\sigma}d + H.C.). \quad (4.2)$$

The momentum of Fermi sea and electron spin are represented by index k, σ, respectively. The leads of left and right are represented by $\alpha \in L, R$. We give new linear-combination operators by conduction electron operators,

$$C^e_{k\sigma} = \frac{C^L_{k\sigma} + C^R_{k\sigma}}{\sqrt{2}}, \qquad C^0_{k\sigma} = \frac{C^L_{k\sigma} - C^R_{k\sigma}}{\sqrt{2}}. \quad (4.3)$$

The first term of Eq.(4.2), $\epsilon_{k\sigma}(C^{L\dagger}_{k\sigma}C^L_{k\sigma} + C^{R\dagger}_{k\sigma}C^R_{k\sigma})$ becomes $\epsilon_{k\sigma}(C^{e\dagger}_{k\sigma}C^e_{k\sigma} + C^{0\dagger}_{k\sigma}C^0_{k\sigma})$. The last term of Eq.(4.2) which represents hybridization of leads and dot becomes $V^\alpha_{k\sigma}(C^{e\dagger}_{k\sigma}d + d^\dagger C^e_{k\sigma})$. The full Hamiltonian can be rewritten as

$$H = \sum_{k\sigma} \epsilon_{k\sigma}(C^{e\dagger}_{k\sigma}C^e_{k\sigma} - \mu_\alpha) + \sum_{k\sigma} \epsilon_{k\sigma}(C^{0\dagger}_{k\sigma}C^0_{k\sigma} - \mu_\alpha) + \quad (4.4)$$
$$\sum_{\sigma} \epsilon_\sigma d^\dagger_\sigma d_\sigma + \frac{U}{2}\sum_{\sigma} \epsilon_d d^\dagger_\sigma d_\sigma + \sum_{k\sigma}(V^\alpha_{k\sigma}C^{e\dagger}_{k\sigma}d + H.C.),$$

where no hybridization coupling between operator d_σ and $C^0_{k\sigma}$. The second term of Eq.(4.4) has no contribution to the quantum dot. There is no second channel contribution to the quantum dot, there is single channel case in this system. The condition for two-channel Kondo effect is that two independent electron reservoirs exist, and there is

no scattering between two conduction electron band of reservoirs. Otherwise, we can use a linear-combination transformation to rewrite the Hamiltonian, and there is only single channel contribution to the quantum dot. The two-channel Kondo model out of equilibrium is shown in Fig.3.1, two electron leads coupled to a quantum dot are two-channel leads, respectively, where Hamiltonian can be written as

$$H = \sum_{\tau,\alpha,\sigma,k} (\epsilon_{k\sigma} - \mu_\alpha) c^{\alpha\dagger}_{k\sigma\tau} c^{\alpha}_{k\sigma\tau} + \sum_{\sigma} \epsilon_\sigma d^\dagger_\sigma d_\sigma + \frac{U}{2} \sum_{\sigma} \epsilon_d d^\dagger_\sigma d_\sigma + \sum_{\tau,\alpha,\sigma,k} (V^{\alpha}_{k\sigma\tau} c^{\alpha\dagger}_{k\sigma\tau} d_\sigma + H.C.). \quad (4.5)$$

Here, we add a new channel index $\tau \in 1, 2$, and we assume hybridization $V^{\alpha}_{k\sigma\tau}$ for different chemical potentials are the same. Simplicity, we set $V^{L}_{k\sigma 1} = V^{R}_{k\sigma 1} = V^{L}_{k\sigma 2} = V^{R}_{k\sigma 2}$ in our study. Theoretically, two-channel Kondo lead can comes from two degenerate states in momentum space [19, 20, 23, 6], or two independent Dirac core in doped graphene citegnauck37. The two channel Kondo has been realized by a quantum dot couple to a finite reservoir and two electron leads come from the other reservoir [16]. Note that: doped graphene is two-channel Kondo system in our study.

Bibliography

[1] L. Kouwenhoven and L. Glazman, Phys. World **14**, 33 (2001).

[2] N. Andrei, K. Furuya, and J. H. Lowenstein, Rev. Mod. Phys. **55** (1983), no. 2, 331-402.

[3] D. L. Cox and A. Zawadowski, Advances in Physics **47** (1998), no. 5, 599-942.

[4] D. L. Cox and A. Zawadowski, Journal of Physics: Condensed Matter **8** (1996), 9825-9853.

[5] A. C. Hewson, *The Kondo Problem to Heavy Fermions*, Cambridge University Press, Cambridge (1997).

[6] Laila Souza de Mattos , *Correlated Electrons Probed By Scanning Tunneling Microscopy.*

[7] W. J. D. Haas and G. J. V. D. Berg, **3** (1936), no. 6, 440 -449.

[8] J. Kondo, Progress of Theoretical Phys **32**, 1 (1964).

[9] Zener, Phys. Rev. **81** (1951) 440.

[10] B. Coqblin, J. R. Schrieffer, Phys. Rev. **185** (1969) 847.

[11] P. W. Anderson, J. Phys. 3, 2436 (1970); P. W. Anderson, Phys. Rev. **124**, 41 (1961).

[12] J. R. Schrieffer and P. A. Wolff, Relation between the Anderson and Kondo Hamiltonians, Physical Review **149** (1966 Sep), no. 2, 491-492.

[13] D. Goldharber-Gorden, Nature (London) **391**, 156 (1998).

[14] D. Goldharber-Gorden, Phys. Rev. Lett. **81**, 5255 (1998).

[15] D. Goldharber-Gorden *et. al.* Material Science and Engineering B **84**, 17-21 (2001).

[16] R. M. Potok, C. I. G. Rau Hadas Shtrikman, Yuval Oreg, and D. Goldhaber-Gorden, Nature (2007)

[17] S. M. Cronenwett, Science **281**, 540 (1998)

[18] M. A. Kastner, Rev. Mod. Phys. **64**, 849 (1975)

[19] A. Zawadowski, Kondo-like state in a simple model for metallic glasses, Physical Review Letters **45** (1980), no. 3, 211.

[20] Nozieres, P. Blandin, A. Kondo effect in real metals. Journal de Physique **41**, 193 211 (1980).

[21] JC-Cuevas, Molecular-electronics-lecture 2.

[22] Henrik Bruus and Karsyen Flensberg, *Many-Body Quantum Theory In Condensed Matter Physic* (2004).

[23] P. Nozieres and A. Blandin, Kondo effect in real metals, Journal de Physique **41** (1980), 193-211.

[24] The website of Goldhaber-Gorden group, **http://www.stanford.edu/group/GGG/kondo.htm**

[25] Cox, D. L. , Phys. Rev. Lett. **59** 1240 (1987).

[26] Seaman, C. L. *et. al.* , Phys. Rev. Lett. **67** 2882 (1991).

[27] Besnus, M. J., *et. al.*, Journal of Magnetism and Magnetic Materials **76-77** 471 (1988).

[28] N. Andrei and C. Destri, Solution of the multichannel Kondo problem, Physical Review Letters **52** (1984), no. 5, 364.

[29] I. Affleck and A. W. W. Ludwig, Exact conformal-field-theory results on the multi-channel Kondo effect: Single-fermion Green's function, self-energy, and resistivity, Physical Review B **48** (1993), no. 10, 7297.

[30] Ralph D.C. and Burhman R. A., Phys. Rev. Lett. **69** 2118 (1992).

[31] Ralph D.C. *et. al.* , Phys. Rev. Lett. **72** 1064 (1994).

[32] Affleck I. and Ludwig A. W. W., Phys. Rev. B **48** 7297 (1993).

[33] Andrei N. and Destri, C., Phys. Rev. Lett. **52** 364 (1984).

[34] Haldane F. D. M. , Phys. Rev. Lett. **40** 416 (1978).

[35] D. C. Ralph, A. W. W. Ludwig, J. von Delft, and R. A. Buhrman, 2-channel Kondo scaling in conductance signals from 2-level tunneling systems, Physical Review Letters **72** (1994), no. 7, 1064-1067.

[36] Subir Sachdev, *Quantum Phase transition*, 2nd Edition.

[37] N. J. Craig, J. M. Taylor, E. A. Lester, C. M. Marus, M. P. Hanson, A. C. Gorssard, Science **304**, 565 (2004)

[38] R. M. Potok, *Probing many body effects in semiconductor nano-structures*, Ph.D. dissertation, Harvard University, 2006.

[39] Gergely Zerand, *et. al.*, Phys. Rev. Lett.**97**, 166802

[40] Gergely Zarand, Chung-Hou Chung, Pascal Simon and Matthias Vojta, PRL. **97**. 166802

[41] Matthias Vojta, Lars Fritz and Ralf Bulla, Europ. Phys. Lett. **90**, 27006 (2010)

[42] K. Sengupta and G. Baskaran, Phys. Rev.B **77**, 045417 (2008)

[43] Lars Fritz and Matthias Vojta, Phys. Rev.B **70**, 214427 (2004)

[44] Imke Schneider, Lars Fritz, Frithjof B. Anders, Adel Benlagra, and Matthias Vojta, PRB **84**. 125139 (2011)

[45] C. Gonzalez-Buxton and K. Ingersent, Phys. Rev. B **57**, 14 254 (1998).

[46] K. Ingersent and Q. Si, Phys. Rev. Lett. **89**, 076403 (2002)

[47] R. Bulla, T. Pruschke, and A. C. Hewson, J. Phys. : Condens. Matter **9**, 10, 463 (1997); R. Bulla, M. T. Glossop, D. E. Logan and T. Pruschke, ibid. **12**, 4899 (2000).

[48] D. Withoff and E. Fradkin, Phys. Rev. Lett. **64**, 1835 (1990). C. R. Cassanello and E. Fradkin, Phys. Rev. B **53**, 15 079 (1996); **6**, 11, 246 (1997). A. Polkovnikov, Phys. Rev. B **65**, 064503 (2002).

[49] Anderson *et. al.* , PRB **1**, 4464 (1970); PRB **1**, 1522 (1970).

[50] K.G. Wilson, phys, Rev.B **4**, 3174. Phys. Rev. B **4**, 3184 (1971)

[51] K.G. Wilson, Rev. Mod.Phys. **47**, 773 (1975); for a review see: R. Bulla, *et. a*l. cond-mat/ 0701105 (2007)

[52] R.C. Ashoori, Nature **379**, 413 (1996)

[53] N. Andrei, Phys. Rev. Lett. **45**, 379 (1980); P. B. Wiegmann, Adv. Phys. **32**, 453; N. Andrei, K.Furuya, J. H. Lowenstein, Rev.Mod. Phys. **55**, 331.

[54] I. Affleck, A.W.W. Ludwig, PRB. **48**, 7297 (1993).

[55] N. Andrei, Phys. Rev. Lett. **45**, 379 (1980); P. B. Wiegmann, J. Phys. C **14**, 1463 (1981); N. Kawakami and A. Okiji, Phys. Lett. A 86, 483 (1981);P. B. Wiegmann and A. M. Tsvelik, JETP Lett. 38, 591 (1983); N. Andrei and C. Destri, Phys. Rev. Lett. **52**, 364 (1984).

[56] H. R. Krishnamurthy, J. W. Wilkins, and K. G. Wilson, Phys. Rev. B **21**, 1003 (1980); **21**, 1044 (1980); H. O. Frota and L. N. Oliveira, Phys. Rev. B **33**, 7871 (1986)

[57] Ned S. Wingreen, Yigal Meir, PRB **47**, no. 15, 10020-10023, (1993)

[58] M.H. Hwttler, J. Kroha, and S. Hershfield, Phys. Rev. B. **73**.14 (1997)

[59] G. D. Mahan, *Many-Particle Physics*, 2nd ed. (Plenum, New York, 1990).

[60] Tsung-Han Lee, Kenneth Yi-Jieh Zhang, Chung-Hou Chung, Stefan Kirchner, arXiv

[61] Farzaneh Zamani, Tathagata Chowdhury, Pedro Ribeiro, Kevin Ingersent, Stefan Kirchner, arXiv

[62] P. Coleman, Phys. Rev. B. **29**, 3035 (1984).

[63] N. E. Bickers, Rev. Mod. Phys. **59**, 845 (1987).

[64] David Withoff and Eduardo Fradkin, Phys. Rev. Lett. **64**, 2835 (1990)

[65] K. Ingersent and Q. Si, Phys. Rev. lett. **89**, 076403 (2002).

[66] Matthew Glossop *et.al.* , Phys. Rev. Lett. **107**, 076404 (2011)

[67] K. S. Novoselov *et. al.* , Science **306**, 666 (2004) , K. S. Novoselov *et. al.* , Nature **438**, 197 (2005) , A. H. Castro Neto *et. al.*, Rev. Mod. Phys. **81**, 109 (2009).

[68] K. Sengupta and G. Baskaran, Phys. Rev.B **77**, 045417 (2008).

[69] Zhen-Gang Zhu, Kai-He Ding, and Jamal Berakdar, Eur. Phys. Lett. **90**, 67001 (2010).

[70] Luca Dell'Anna, J. Stat. Mech. P 01007 (2010).

[71] M.H. Hwttler, J. Kroha, and S. Hershfield, Phys. Rev. Lett. **73**. 14 (1994).

[72] Yigal Meir, Ned S. Wingreen. Physical Review Letters, Vol. **68**, No. 16. 2512-2515.